

Electronic structure of [001]- and [111]-growth-axis semiconductor superlattices

C. Mailhot

Xerox Corporation, Webster Research Center (0114-41D), 800 Phillips Road, Webster, New York 14580

D. L. Smith

Los Alamos National Laboratory, University of California, P.O. Box 1663, Los Alamos, New Mexico 87545

(Received 25 August 1986)

A $\mathbf{k}\cdot\mathbf{p}$ theory is used to investigate the electronic structure of semiconductor superlattices grown along the [001] and [111] axes. The present work considers the case of $\text{Ga}_{1-x}\text{In}_x\text{As}-\text{Al}_{1-y}\text{In}_y\text{As}$ superlattices. We specifically treat three alloy composition pairs: a lattice-matched case ($x=0.53$, $y=0.52$), a case where the Ga-containing layers are in biaxial tension with a 0.8% lattice mismatch ($x=0.53$, $y=0.64$), and a case where the Ga-containing layers are in biaxial compression with a 1.5% lattice mismatch ($x=0.53$, $y=0.30$). We analyze the effects of the growth axis on the electronic structure of the superlattice from a consideration of the subband dispersion both parallel and perpendicular to the growth direction. Apart from point-group symmetry considerations, a major factor which differentiates the electronic structure of [001]- and [111]-growth-axis superlattices is the presence of large (exceeding 100 kV/cm) internal strain-induced electric fields in strained-layer superlattices grown along the [111] axis. These internal electric fields are directed along the [111] growth axis and are generated by the internal strain because the constituent semiconductors are piezoelectric. In [001]-growth-axis strained-layer superlattices, the orientation of the lattice-mismatch-induced strains is such that these fields are not present. We demonstrate that the strain-induced electric fields result in sizeable Stark shifts on the superlattice electron and hole subbands and lead to a substantial reduction of the superlattice band gap. Moreover, these strain-induced internal electric fields modify the superlattice wave functions and cause a spatial separation of electrons and holes within the confining superlattice layers. This latter effect greatly modifies the interband optical matrix elements. It also leads to a screening of the strain-induced internal electric fields by photogenerated free carriers which causes nonlinear (i.e., intensity-dependent) optical response of [111]-growth-axis strained-layer superlattices.

I. INTRODUCTION

Semiconductor superlattices are made by the alternating epitaxial growth of thin layers of two semiconductors with approximately (i.e., to within a few percent) the same lattice constant.¹ Superlattices in which both semiconductors are III-V, II-VI, or group-IV zinc-blende structure materials are currently being grown by molecular-beam epitaxy and metal-organic chemical vapor deposition.¹ Such artificial structures are currently of great technological interest because they afford the possibility of tailoring the electronic structure of the resulting system by controlled modifications of the growth parameters (layer thicknesses, alloy compositions, growth axis, strain, etc.). The flexibility at tuning the electronic band structure of semiconductor superlattices is currently being exploited through the novel design of semiconductor diode lasers,² electro-optical modulators,³ nonlinear optical devices,⁴ infrared imaging systems,⁵ etc. In the case where the constituent semiconductors have somewhat different lattice constants, it is possible to accommodate the lattice mismatch by uniform internal strain rather than by the generation of dislocations, provided the individual layers are grown thin enough (typically less than 250 Å).⁶ It has

been demonstrated that these strained-layer superlattices can be grown with a high degree of crystalline perfection.⁷⁻⁹

The possibility of modifying the electronic structure of semiconductor superlattices according to variations in the layer thickness of the constituent semiconductors is well documented.¹ However, little is known about the effects of the growth orientation on the electronic structure of semiconductor superlattices. This lack of knowledge apparently has its origin in the fact that, until recently, most III-V semiconductor superlattices have been grown along the [001] axis. Likewise, most studies of strained-layer superlattices have been performed for III-V semiconductor systems with the growth axis being along a [001] direction. However, the epitaxial growth of III-V semiconductor heterojunctions along various crystallographic axes has recently been demonstrated.¹⁰ Moreover, II-VI semiconductor superlattices are currently being grown along the [111] axis.¹¹⁻¹³ A study of strained-layer semiconductor superlattices grown along various crystallographic orientations is therefore desirable and timely since these systems are now being experimentally investigated.

The purpose of this paper is to demonstrate that strained-layer superlattices grown along the [111] axis ex-

hibit major features not found in [001]-growth-axis strained-layer superlattices. Foremost among these differences is the presence of strain-induced polarization fields in the layers of [111]-growth-axis superlattices.¹⁴ Indeed, the lattice-mismatch-induced strain in [111]-growth-axis superlattices is piezoelectrically active whereas in [001]-growth-axis superlattices it is not. The magnitude of these strain-induced internal piezoelectric fields can exceed 100 kV/cm, a value typical of breakdown fields in III-V zinc-blende structure compound semiconductors. These internal electric fields produce sizeable Stark shifts of the superlattice energy subbands and consequently modify the electronic properties of [111]-growth-axis strained-layer superlattices with respect to those of their [001] counterparts. In the case where photogenerated free carriers are present to screen the strain-induced electric fields, it is expected that the optical response of [111]-growth-axis superlattices will be strongly nonlinear, i.e., dependent on the intensity of the excitation.

A thorough study of the symmetry-related differences between [001]- and [111]-growth-axis HgTe-CdTe superlattices has recently appeared in the literature.¹⁵ This system is characterized by a lattice mismatch of only 0.3% and consequently the effects of strain-induced internal fields were neglected in Ref. 15. Application of our model to a point-group symmetry analysis of [001]- and [111]-growth-axis HgTe-CdTe superlattices¹⁶ yields results in quantitative agreement with those reported in Ref. 15.

Our analysis of the electronic structure of [111]- and [001]-growth-axis semiconductor superlattices is based on a $\mathbf{k}\cdot\mathbf{p}$ theory of semiconductor heterointerfaces. A description of the superlattice wave function is formulated in terms of a linear combination of propagating and evanescent bulk Bloch states of the constituent semiconductors. These bulk Bloch states are generally associated with complex values of the component of the crystal wave vector parallel to the superlattice growth axis. A single expansion set of zone-center ($\mathbf{k}=\mathbf{0}$) basis functions, derived from an average reference pseudopotential Hamiltonian, is used to describe the bulk Bloch states of the constituent semiconductors. A distinctive feature of the present $\mathbf{k}\cdot\mathbf{p}$ model is the correct description of superlattice energy band mixing, band crossings, and band splittings for superlattice wave vectors parallel or perpendicular to the growth axis. A correct description of the superlattice point-group symmetry is an essential ingredient to a meaningful analysis of the effects of the growth orientation on the electronic structure of the superlattice. Moreover, since a pseudopotential formalism is used to generate the (single) basis set of zone-center functions, momentum matrix elements are explicitly calculated in a plane-wave representation. Consequently, the number of empirical parameters is reduced to a knowledge of pseudopotential form factors.

In the case of lattice-mismatched superlattices, the effects of the resulting internal strain on the superlattice electronic band structure are also investigated. This is accomplished by a deformation potential description of the bulk band structure of each constituent semiconductor under the influence of a lattice-mismatch-induced internal

strain. In the case of [111]-growth-axis strained-layer superlattice, the effects of strain-induced electric fields are incorporated by an extension of our basic $\mathbf{k}\cdot\mathbf{p}$ model to include slowly varying potentials.

For illustrative purposes, we consider $\text{Ga}_{1-x}\text{In}_x\text{As}-\text{Al}_{1-y}\text{In}_y\text{As}$ superlattices grown along the [001] and [111] crystallographic axes. One motivation for studying this system lies in its potential application in the field of optical communications.¹⁷ This material system also has the feature that the small band-gap (carrier confining) Ga-containing alloy can either be under biaxial tension or compression by proper choice of alloy compositions. Moreover, $\text{Ga}_{1-x}\text{In}_x\text{As}-\text{Al}_{1-y}\text{In}_y\text{As}$ superlattices are currently being epitaxially grown on InP[100] substrates for an alloy composition which exhibits lattice matching with this substrate, i.e., $x=0.53$ and $y=0.52$.¹⁸⁻²²

The paper is organized as follows: in Sec. II we briefly review the theoretical formalism which serves as the basis for the calculation of the electronic structure of semiconductor superlattices. Results relating to lattice-matched $\text{Ga}_{0.47}\text{In}_{0.53}\text{As}-\text{Al}_{0.48}\text{In}_{0.52}\text{As}$ superlattices are presented in Sec. III. The electronic structures of superlattices grown along the [001] and [111] axes are presented and point-group symmetries are discussed. In Sec. IV, we present results for strained-layer $\text{Ga}_{1-x}\text{In}_x\text{As}-\text{Al}_{1-y}\text{In}_y\text{As}$ superlattices. Special attention is given to the effects of strain-induced internal piezoelectric fields on the electronic structure and optical matrix elements of [111]-growth-axis superlattices. Applications involving nonlinear optical response arising from screening of these strain-induced electric fields by (photogenerated) free carriers are also considered in this section. We conclude with a synopsis in Sec. V.

II. THEORETICAL FORMALISM

The electronic structure calculations presented below are based on a $\mathbf{k}\cdot\mathbf{p}$ formalism designed to treat semiconductor heterojunctions and superlattices.²³ At a general \mathbf{k} point (near $\mathbf{k}=\mathbf{0}$) the bulk Bloch states in each semiconductor are expanded to first order in terms of zone-center ($\mathbf{k}=\mathbf{0}$) basis functions associated with a *single* reference Hamiltonian. This feature is essential to a correct description of the superlattice point-group symmetry. The expansion set is explicitly derived from a reference pseudopotential Hamiltonian obtained by averaging the bulk pseudopotentials of the constituent semiconductors. Since the pseudopotentials associated with the constituent semiconductors are different, the operator treated as a perturbation in semiconductor i ($i=A,B$) is

$$H_{\text{pert}}^{(i)}(\mathbf{k}) = \frac{\hbar}{m} \mathbf{k}\cdot\mathbf{p} + \Delta V^{(i)}(\mathbf{x}), \quad (1a)$$

where \mathbf{k} is the crystal wave vector, \mathbf{p} is the momentum operator and $\Delta V^{(i)}(\mathbf{x})$ is the difference between the pseudopotential of semiconductor i and that of the reference Hamiltonian,

$$\Delta V^{(i)}(\mathbf{x}) \equiv V^{(i)}(\mathbf{x}) - V^{\text{ref}}(\mathbf{x}), \quad (1b)$$

with

$$V^{\text{ref}}(\mathbf{x}) = \frac{1}{2} [V^{(A)}(\mathbf{x}) + V^{(B)}(\mathbf{x})]. \quad (1c)$$

In the present $\mathbf{k}\cdot\mathbf{p}$ treatment the zone-center states of the reference Hamiltonian belonging to the irreducible representations Γ_7 , Γ_8 , and Γ_6 of the T_d double group are treated explicitly. Löwdin perturbation is used to include an additional 46 zone-center states (including spin) and to calculate higher-order $\mathbf{k}\cdot\mathbf{p}$ momentum matrix elements.

The bulk Bloch solutions associated with complex wave vector \mathbf{k} in material i are given to first order in perturbation theory, by

$$\Psi^{(i)}(\mathbf{k}; \mathbf{x}) = \exp(i\mathbf{k}\cdot\mathbf{x}) \sum_d |d; \mathbf{k}; i\rangle C^{(i)}(d, \mathbf{k}), \quad (2a)$$

with

$$|d; \mathbf{k}; i\rangle \equiv |d\rangle + \sum_{\beta} |\beta\rangle \frac{\langle \beta | (\hbar/m)\mathbf{k}\cdot\mathbf{p} + \Delta V^{(i)} | d \rangle}{(\varepsilon_d - \varepsilon_{\beta})}. \quad (2b)$$

The explicitly treated zone-center functions $u_d(\mathbf{x}) \equiv \langle \mathbf{x} | d \rangle$ span the eight-dimensional subspace of the irreducible representations Γ_7 , Γ_8 , and Γ_6 . The 46 zone-center basis functions $u_{\beta}(\mathbf{x}) \equiv \langle \mathbf{x} | \beta \rangle$ are treated in Löwdin perturbation theory. In Eq. (2), ε_d (ε_{β}) are the zone-center energies of the basis functions $|d\rangle$ ($|\beta\rangle$) of the reference Hamiltonian.

The expansion coefficients $C^{(i)}(d, \mathbf{k})$ in Eq. (2a) are obtained by solving the secular equation

$$[H^{(i)}(d, d'; \mathbf{k}) - E\delta_{d,d'}] C^{(i)}(d', \mathbf{k}) = 0, \quad (3a)$$

where the Hamiltonian matrix is

$$H^{(i)}(d, d'; \mathbf{k}) = [\varepsilon_d + (\hbar^2/2m) |\mathbf{k}|^2] \delta_{d,d'} + \langle d | (\hbar/m)\mathbf{k}\cdot\mathbf{p} | d' \rangle + \langle d | \Delta V^{(i)} + H_{\text{s.o.}}^{(i)} + H_{\text{st}}^{(i)} | d' \rangle + \sum_{\beta} \frac{\langle d | (\hbar/m)\mathbf{k}\cdot\mathbf{p} + \Delta V^{(i)} | \beta \rangle \langle \beta | (\hbar/m)\mathbf{k}\cdot\mathbf{p} + \Delta V^{(i)} | d' \rangle}{\frac{1}{2}(\varepsilon_d + \varepsilon_{d'}) - \varepsilon_{\beta}}. \quad (3b)$$

Here $H_{\text{s.o.}}^{(i)}$ and $H_{\text{st}}^{(i)}$ describe the spin-orbit and strain interactions in material i , respectively, and E is the energy of the Bloch state. For a description of an interface, the component of the wave vector \mathbf{k} perpendicular to the interface is in general complex.

In previous models based on the $\mathbf{k}\cdot\mathbf{p}$ formalism,^{24–26} the zone-center energy eigenstates of the two constituent semiconductors are assumed to be the same. This assumption is equivalent to including $\Delta V^{(i)}$ only to first order in energies and zeroth order in the wave functions. We include $\Delta V^{(i)}$ to second order in energies and first order in wave functions. Neglecting $\Delta V^{(i)}$ in the wavefunction description introduces more symmetry in the model than the physical system actually has. As a result, energy-band crossings, mixings, and splittings are not properly described.

A description of the superlattice wave function is formulated in terms of a linear combination of bulk propagating (\mathbf{k} real) and evanescent (\mathbf{k} complex) states of the constituent semiconductors, $\Psi^{(i)}(\mathbf{k}; \mathbf{x})$ [Eq. (2)]. Interface matching of the constituent material bulk eigenfunctions is accomplished using results derived about the component of the current-density operator parallel to the growth axis.²³ Superlattice translational symmetry is used to derive an eigenvalue equation for the superlattice wave vector and eigenfunctions.

Calculations are carried out to first order in $H_{\text{pert}}^{(i)}(\mathbf{k})$ for wave functions and current densities and second order in $H_{\text{pert}}^{(i)}(\mathbf{k})$ for energies. Spin-orbit and stress interactions are included between the explicitly included states: Γ_7 , Γ_8 , and Γ_6 . The momentum matrix elements appearing in Eq. (3b) are explicitly calculated from a pseudopotential plane wave representation of the reference Hamiltonian. Therefore, the input parameters are the pseudopotential

form factors of the constituent semiconductors and consequently our model does not require an empirical knowledge of momentum matrix elements. A set of pseudopotential form factors which provide a good description of the bulk band structure of GaAs, AlAs, and InAs is given in Ref. 23. A modified virtual-crystal approximation²⁷ is used to obtain the empirical pseudopotential form factors of the alloys $\text{Ga}_{1-x}\text{In}_x\text{As}$ and $\text{Al}_{1-y}\text{In}_y\text{As}$ from a knowledge of the corresponding quantities in GaAs, AlAs, and InAs. The reference pseudopotential Hamiltonian²³ is expressed in a plane-wave basis (113 plane waves are included) and diagonalized at $\mathbf{k}=\mathbf{0}$. The resulting zone-center energy eigenstates ($|d\rangle$, $|\beta\rangle$) and eigenvalues (ε_d , ε_{β}) are used to evaluate the matrix elements of $H^{(i)}(d, d'; \mathbf{k})$ in Eq. (3b). These matrix elements are listed in Table I for the alloys $\text{Ga}_{1-x}\text{In}_x\text{As}$ and $\text{Al}_{1-y}\text{In}_y\text{As}$ corresponding to the composition pairs ($x=0.53, y=0.52$), ($x=0.53, y=0.30$), and ($x=0.53, y=0.64$). A definition of the matrix elements appearing in Table I can be found in Appendix I of Ref. 23 using the nomenclature of Ref. 28

The energy line-up (energy-band offset) constitutes an empirical input to our model and is extracted from recent current-voltage profiling measurements on $\text{Ga}_{1-x}\text{In}_x\text{As}-\text{Al}_{1-y}\text{In}_y\text{As}$ heterojunctions¹⁷ at the lattice-matched alloy composition, $x=0.53$ and $y=0.52$. This work shows that the ratio of the conduction-band offset (ΔE_c) to the difference in band gap between $\text{Ga}_{0.47}\text{In}_{0.53}\text{As}$ and $\text{Al}_{0.48}\text{In}_{0.52}\text{As}$ (ΔE_g) is of the order of (0.71 ± 0.07) . For the present purposes, a value of $\Delta E_v = \Delta E_g - \Delta E_c = 0.315\Delta E_g$ was adopted for the magnitude of the valence-band offset for all alloy compositions studied. In the determination of ΔE_v , the quantity ΔE_g represents the band-gap difference between the unstressed alloys.

TABLE I. Numerical values (in Rydberg atomic units) of various matrix elements used in the evaluation of the bulk Hamiltonian and current density matrices for $\text{Ga}_{1-x}\text{In}_x\text{As}-\text{Al}_{1-y}\text{In}_y\text{As}$ superlattices. The matrix elements are defined in Appendix I of Ref. 23 and are evaluated using the zone-center energy eigenstates and eigenvalues of the reference Hamiltonian. Energy band gaps are expressed in eV.

	$x=0.53$ $y=0.52$	$x=0.53$ $y=0.64$	$x=0.53$ $y=0.30$
A'	-5.17×10^{-2}	-5.42×10^{-2}	-4.68×10^{-2}
B	4.48×10^{-2}	4.79×10^{-2}	4.34×10^{-2}
P	1.10	1.09	1.11
L'	-1.40	-1.39	-1.42
M	-2.92	-2.89	-2.96
N'	-1.80	-1.79	-1.86
$\Delta\epsilon_s^{(A)}$	-2.26×10^{-2}	-1.36×10^{-2}	-4.06×10^{-2}
$\Delta\epsilon_p^{(A)}$	3.85×10^{-3}	1.31×10^{-3}	8.88×10^{-3}
$\Delta P^{(A)}$	2.48×10^{-3}	4.84×10^{-4}	5.60×10^{-3}
$i\Delta_{SZ}$	1.38×10^{-3}	7.83×10^{-4}	2.36×10^{-3}
$i\Delta_{ZS}$	-6.34×10^{-3}	-1.75×10^{-3}	-1.36×10^{-2}
$i\Delta_{xy}$	-1.65×10^{-2}	-1.40×10^{-2}	-2.21×10^{-2}
$E_g(\text{Ga}_{1-x}\text{In}_x\text{As})$	0.79	0.79	0.79
$E_g(\text{Al}_{1-y}\text{In}_y\text{As})$	1.52	1.20	2.15

III. LATTICE-MATCHED SUPERLATTICES

In this section, we investigate the electronic structure of $\text{Ga}_{0.47}\text{In}_{0.53}\text{As}-\text{Al}_{0.48}\text{In}_{0.52}\text{As}$ superlattices grown along the [001] or the [111] axis. Such superlattices are lattice-matched to a $\text{InP}[100]$ substrate and are currently being investigated for their potential application in optical communication systems.¹⁷⁻¹⁹ We emphasize the difference in electronic structure arising from the different point-group symmetries between [001]- and [111]-growth-axis superlattices. Detailed considerations of strain-induced effects are given in the following section.

A. [001]-growth-axis superlattices

Figure 1 shows the electronic band structure of a [001]-growth-axis superlattice consisting of 70 Å of $\text{Ga}_{0.47}\text{In}_{0.53}\text{As}$ alternating with 30 Å of $\text{Al}_{0.48}\text{In}_{0.52}\text{As}$. Superlattice subband dispersion is shown for superlattice wave vectors both parallel ($Q \sim [001]$) and perpendicular ($k_x \sim [100]$) to the [001]-growth axis. Subbands are labeled according to their dominant bulk state component: conduction (C), heavy-hole (HH), and light-hole (LH). Spin split-off hole subbands (SOH) are not shown here.

In [001]-growth-axis superlattices, the T_d point-group symmetry associated with bulk zinc-blende structure compound semiconductors is reduced to D_{2d} . The symmetry elements which survive consist of a fourfold rotoinversion axis ($Q \sim [001]$), two twofold rotation axes ($k_x \sim [100]$ and $k_y \sim [010]$), and two mirror planes containing the fourfold axis and bisecting the angles between the twofold axes. There are two twofold irreducible representations of D_{2d} compatible with spin: Γ_6 and Γ_7 .^{29,30} The odd-number conduction-band states (C_1, C_3, \dots), the odd-number heavy-hole band states ($\text{HH}_1, \text{HH}_3, \dots$) and the even-number light-hole band states ($\text{LH}_2, \text{LH}_4, \dots$) transform like Γ_6 whereas the even-number conduction

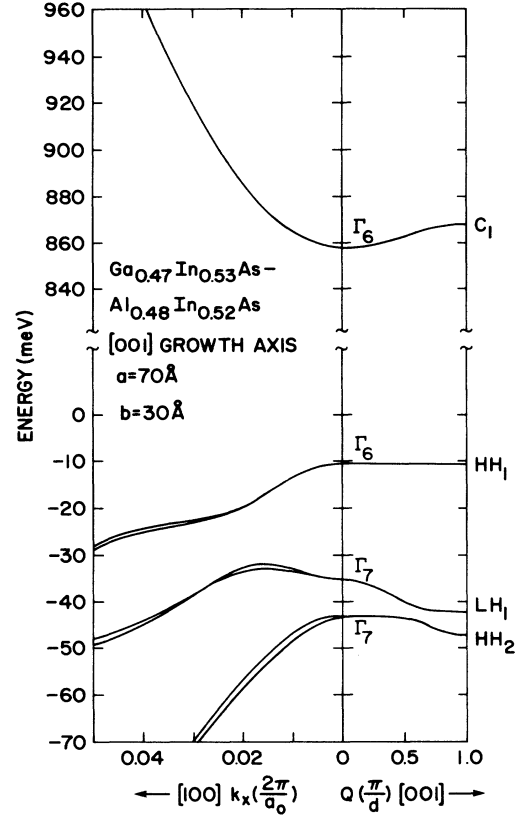


FIG. 1. Electronic energy band structure of a [001] lattice-matched superlattice consisting of 70 Å of $\text{Ga}_{0.47}\text{In}_{0.53}\text{As}$ alternating with 30 Å of $\text{Al}_{0.48}\text{In}_{0.52}\text{As}$. The energy zero coincides with the valence-band maximum of the bulk $\text{Ga}_{0.47}\text{In}_{0.53}\text{As}$ alloy.

and heavy-hole band states and the odd-number light-hole band states transform like Γ_7

For superlattice wave vectors directed along the [001] growth axis ($\mathbf{k}_{\parallel}=\mathbf{0}$; $Q\neq 0$), the factor group is C_{2v} . The double group contains a single two-dimensional representation, Γ_5 .^{29,30} Therefore all bands are twofold degenerate and crossing of superlattice subbands is forbidden along this direction. This symmetry-induced anticrossing behavior along the [001] growth axis is clearly shown in Fig. 1 for the hole subbands LH_1 and HH_2 . The present $\mathbf{k}\cdot\mathbf{p}$ model is able to reproduce this anticrossing behavior through the inclusion of the term $\Delta V^{(i)}(\mathbf{x})$ [Eq. (1b)] in the expression of the current-density matrices used in the interfacial boundary conditions.²³ In prior $\mathbf{k}\cdot\mathbf{p}$ models, where the zone-center states in the two constituent materials are assumed to be the same, such mixing is not described and the bands LH_1 and HH_2 would cross in these models.

In the case where the superlattice wave vector lies in the plane of the interface along one of the twofold axis the factor group is reduced to C_2 . The group C_2 contains two one-dimensional representations compatible with spin: Γ_3 and Γ_4 .²⁹ Subband crossing is allowed in this direction for superlattice subbands belonging to different irreducible representations. For \mathbf{k}_{\parallel} in the [110] and $[1\bar{1}0]$ directions, the factor group is C_5 . For \mathbf{k}_{\parallel} in other directions, all spatial symmetry is lost. The lack of inversion symmetry in [001]-growth-axis superlattices made from zinc-blende structure compound semiconductors produces a splitting of the Kramers doublet throughout the superlattice Brillouin zone, except along the [001] growth axis.³¹ This splitting is proportional to the second-order matrix element coupling the s state of the conduction-band minimum to the p states of the valence-band maximum. If such a matrix element were zero, as is the case for diamond-structure semiconductors with a center of inversion, a twofold Kramers degeneracy would exist throughout the superlattice Brillouin zone by a combination of time-reversal and inversion symmetries.

B. [111]-growth-axis superlattices

In Fig. 2, we show subband dispersions for a [111]-growth-axis superlattice consisting of 70 Å of $\text{Ga}_{0.47}\text{In}_{0.53}\text{As}$ alternating with 30 Å of $\text{Al}_{0.48}\text{In}_{0.52}\text{As}$. We consider superlattice wave vectors with components parallel ($Q\sim[111]$) and perpendicular ($k_x\sim[1\bar{1}0]$) to the [111]-growth direction. The labeling of the subbands refers to the convention adopted for [001]-growth-axis superlattices.

When superlattices consisting of zinc-blende structure compound semiconductors are grown along the [111] axis, the bulk T_d point-group symmetry is reduced to C_{3v} . Thus, for [111]-growth-axis superlattices, the symmetry elements which persist are a threefold rotation axis ($Q\sim[111]$), a mirror plane containing the threefold axis and perpendicular to the $[1\bar{1}0]$ direction ($k_x\sim[1\bar{1}0]$), and two other mirror planes generated by the rotation acting on the first mirror plane. There are three irreducible representations of C_{3v} compatible with spin: Γ_4 , Γ_5 , and Γ_6 . The irreducible representation Γ_4 is twofold degenerate whereas Γ_5 and Γ_6 are one-dimensional. At the zone

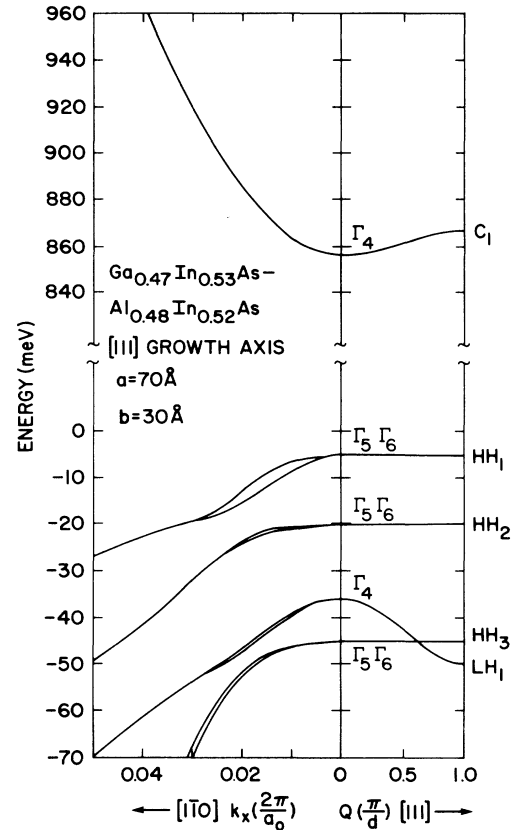


FIG. 2. Electronic energy band structure of a [111] lattice-matched superlattice consisting of 70 Å of $\text{Ga}_{0.47}\text{In}_{0.53}\text{As}$ alternating with 30 Å of $\text{Al}_{0.48}\text{In}_{0.52}\text{As}$. The energy zero coincides with the valence band maximum of the bulk $\text{Ga}_{0.47}\text{In}_{0.53}\text{As}$ alloy.

center Γ_5 and Γ_6 are degenerate by time reversal. The conduction-band states (C_1, C_2, C_3, \dots) and light-hole states (LH_1, LH_2, LH_3, \dots) transform like Γ_4 and the heavy-hole states (HH_1, HH_2, HH_3, \dots) transform like (Γ_5, Γ_6).

For superlattice wave vectors directed along the [111]-growth axis ($\mathbf{k}_{\parallel}=\mathbf{0}$; $Q\neq 0$) the factor group remains the entire C_{3v} point group. While time-reversal symmetry requires that the one-dimensional irreducible representations Γ_5 and Γ_6 be degenerate at the center of the superlattice Brillouin zone ($\mathbf{k}_{\parallel}=\mathbf{0}; Q=0$), these states should in principle split away from the center of the Brillouin zone. However, the interactions which lead to this splitting, \mathbf{k} -dependent spin-orbit interactions, are very small. We have not included these very small terms in the calculation (although it is easy to do so), and therefore the Γ_5 and Γ_6 bands do not split away from $Q=0$ in the calculation. States belonging to the two-dimensional irreducible representation Γ_4 do not mix with those belonging to the (Γ_5, Γ_6) irreducible representations and crossing is allowed for superlattice wave vectors along the [111] growth axis. Such a crossing behavior is reproduced by our $\mathbf{k}\cdot\mathbf{p}$ model as is evident in Fig. 2 for the case of the hole subbands HH_3 and LH_1 .

In the case where the superlattice wave vector lies in the plane of the interface and is in one of the mirror planes ($\mathbf{k}_{\parallel} \sim [11\bar{2}]$, $[1\bar{2}1]$, or $[\bar{2}11]$ and $Q=0$), the factor group is C_S . The group C_S contains two nondegenerate representations compatible with spin. Subband crossing is allowed in these directions for superlattice subbands belonging to different representations. For other directions of \mathbf{k}_{\parallel} , all spatial symmetry is lost. In all cases with $\mathbf{k}_{\parallel} \neq 0$, the subbands are nondegenerate.

Comparing Figs. 1 and 2, one sees many similarities. The conduction and light-hole subbands have very nearly the same zone-center energies for the two growth directions. But the zone-center energies of the heavy-hole bands are significantly higher for the [111]-growth-axis material. (That is, the quantum confinement energy is much less for heavy holes in [111]-growth-axis material than for [001]-growth-axis material.) These results occur because the electron and light-hole effective masses in zinc-blende materials are nearly isotropic whereas the heavy-hole effective mass is larger in the [111] direction than the [001] direction. The electron dispersion is very similar for the two growth direction materials. Hole dispersion in \mathbf{k}_{\parallel} directions are not similar. Light-hole dispersion along the growth axis ($Q \neq 0$) are similar for the two growth axis materials except for cases where the light- and heavy-band energies become close and the bands mix and repel each other for [001]-growth-axis material but do not mix and cross each other for [111]-growth-axis material (see Figs. 1 and 2). The above results, based on point-group symmetry considerations, are fully compatible with those reported in Ref. 15.

C. Symmetry of superlattice zone-center wave functions

We now discuss the symmetry character of the superlattice wave functions at the center of the Brillouin zone ($\mathbf{k}_{\parallel}=0, Q=0$). At the center of the superlattice Brillouin zone, the factor group is equivalent to the entire superlattice point group. We consider, in turn, [001]- and [111]-growth-axis superlattices and we illustrate our discussion by focusing on the first and second light-hole subbands (LH_1 and LH_2) of the superlattices whose subband dispersion are shown in Figs. 1 and 2. The superlattice subband LH_2 is not shown in Figs. 1 and 2, however. A description of the zinc-blende periodic basis functions transforming according to the various irreducible representations at the center of the superlattice Brillouin zone is given in Appendix A.

The superlattice wave functions can be written as

$$\Psi_{Q\alpha}(\mathbf{x}) = \frac{\exp(i\mathbf{Q}\cdot\mathbf{x})}{(N)^{1/2}} \sum_{\beta} \sqrt{l} F_{\beta}^{Q\alpha}(z) u_{\beta}(\mathbf{x}), \quad (4)$$

where $\mathbf{Q} = \mathbf{k}_{\parallel} + \hat{z}Q$ is the superlattice wave vector, α is a set of quantum numbers labeling the superlattice solutions, N is the number of superlattice unit cells, l is the length of a zinc-blende unit cell in the growth direction, and $u_{\beta}(\mathbf{x})$ are the zinc-blende periodic basis functions. The envelope functions $F(z)$ are functions of distance along the growth axis "z" alone because of \mathbf{k}_{\parallel} conservation at the interfaces. They are superlattice periodic functions. Wave function normalization requires

$$\sum_d \int_{-b}^a |F_d(z)|^2 dz = 1, \quad (5)$$

where only the eight explicitly included states are kept in the sum and the integration is across one superlattice unit cell along the growth direction. The superlattice period is $(a+b)$. Explicit expressions for the envelope functions are given in Ref. 23. However, in the definition of the envelope functions used in Eq. (4), a phase $\exp(i\mathbf{Q}\cdot\mathbf{x}) = \exp(i\mathbf{k}_{\parallel}\cdot\mathbf{x}_{\parallel})\exp(iQz)$ has been factored out (see Eqs. 44 of Ref. 23).

At the zone center, the superlattice wave function transforms like one of the irreducible representations of the superlattice point group which is compatible with spin. The zinc-blende periodic functions $u_{\beta}(\mathbf{x})$ can be written as basis functions of these representations. The envelope functions $F_{\beta}(z)$ are functions of z alone. For the D_{2d} point group of a [001]-growth-axis superlattice, a function of z alone can only transform like Γ_1 or Γ_4 . The envelope function $F(z)$ is an even function of z through the center of each material layer if it transforms like Γ_1 and an odd function of z through the center of each material layer if it transforms like Γ_4 . Superlattice translational symmetry ensures that if a function of z is even (odd) through the center of one material layer, it is even (odd) through the center of the other. Since the direct product of Γ_1 with Γ_6 (Γ_7) is Γ_6 (Γ_7) and the direct product of Γ_4 with Γ_6 (Γ_7) is Γ_7 (Γ_6), a zone-center [001] superlattice wave function which transforms like Γ_6 will contain a sum of terms consisting of a Γ_1 envelope function times a Γ_6 zinc-blende periodic function and a Γ_4 envelope function times a Γ_7 zinc-blende periodic function, that is

$$\Psi_{\Gamma_6}^{[001]} = \sum F_{\Gamma_1} u_{\Gamma_6} + \sum F_{\Gamma_4} u_{\Gamma_7}. \quad (6a)$$

Likewise, a zone-center [001] superlattice wave function which transforms like Γ_7 will contain a sum of terms consisting of a Γ_1 envelope function times a Γ_7 zinc-blende periodic function and a Γ_4 envelope function times a Γ_6 zinc-blende periodic function, that is

$$\Psi_{\Gamma_7}^{[001]} = \sum F_{\Gamma_1} u_{\Gamma_7} + \sum F_{\Gamma_4} u_{\Gamma_6}. \quad (6b)$$

The two-dimensional representations Γ_6 and Γ_7 can be chosen so that pairs of basis functions can be labeled "spin up" and "spin down" and the Clebsch-Gordan coefficients for the direct products in Eqs. (6) do not mix these labels.

For the C_{3v} point group of a [111] superlattice, any function of z transforms like Γ_1 . (The symmetry operators of C_{3v} do not change z). Therefore a zone-center [111] superlattice wave function which transforms like Γ_4 (Γ_5 or Γ_6) will contain a sum of terms consisting of an envelope function that transforms like Γ_1 times a zinc-blende periodic function that transforms like Γ_4 (Γ_5 or Γ_6) that is

$$\Psi_{\Gamma_i}^{[111]} = \sum F_{\Gamma_1} u_{\Gamma_i} \quad (i=4, 5, \text{ or } 6). \quad (7)$$

The two-dimensional representation Γ_4 can be chosen so that pairs of basis functions can be labeled spin up and spin down and the sum in Eq. (7) will not mix these labels (for $i=4$).

In Fig. 3, we show the envelope functions multiplying the four explicitly included spin-up basis states for the spin-up LH₁ and LH₂ hole subband zone-center states for the [001]-growth-axis superlattice whose dispersion curves are shown in Fig. 1. The LH₁ state transforms like Γ_7 . The large-amplitude envelope functions which multiply the zinc-blende periodic functions $^1\Gamma_7(z\uparrow)$ and $^2\Gamma_7[(x+iy)\downarrow]$ are even (transform like Γ_1). The $^1\Gamma_7$ and $^2\Gamma_7$ periodic functions combine to make up the $k_z \rightarrow 0$ light-hole (and split-off hole states), in the bulk material. The smaller amplitude envelope functions which multiply the zinc-blende periodic functions $^1\Gamma_6(s\uparrow)$ and $^2\Gamma_6[i(x-iy)\downarrow]$ are odd (transform like Γ_4). The $^1\Gamma_6$ and $^2\Gamma_6$ periodic functions make up the $k_z \rightarrow 0$ conduction and heavy-hole bands, respectively. The inclusion of the $^2\Gamma_6$

periodic-function component in LH₁ is a consequence of the heavy-hole and light-hole mixing which result from the inclusion of terms proportional to $\Delta V^{(i)}$ in the current density matrices.²³ It is the same interaction which causes the mixing of the LH₁ and HH₂ bands evident in Fig. 1. The LH₂ state transforms like Γ_6 . The large-amplitude envelope functions which multiply the $^1\Gamma_7$ and $^2\Gamma_7$ zinc-blende periodic functions are odd whereas the small amplitude envelope functions which multiply the $^1\Gamma_6$ and $^2\Gamma_6$ zinc-blende periodic functions are even. The inclusion of the periodic $^2\Gamma_6$ function component is, again, an example of heavy-hole and light-hole mixing.

In Fig. 4, we show the envelope functions multiplying the explicitly included spin-up Γ_4 basis states for the spin-up LH₁ and LH₂ hole subband zone-center states for

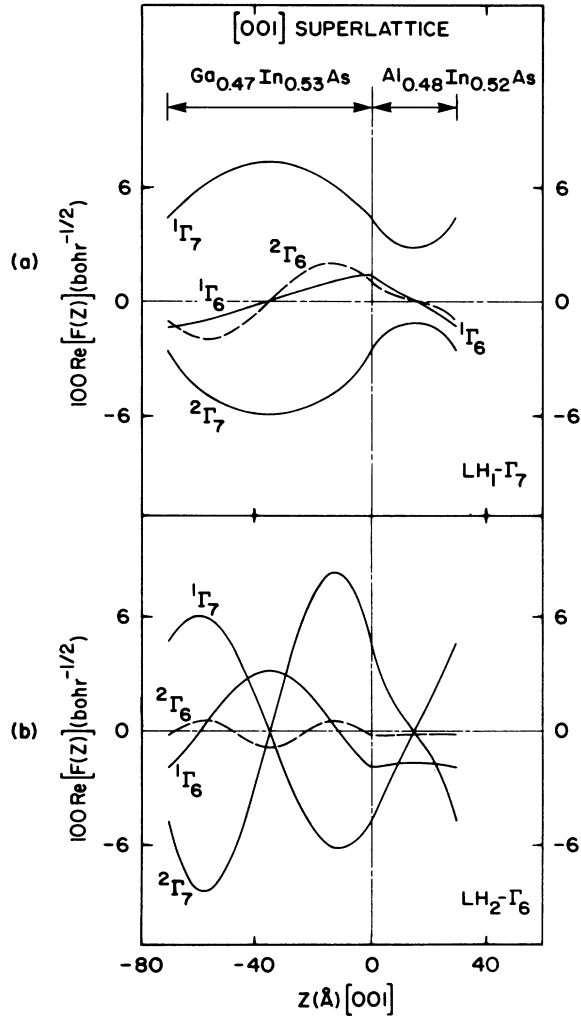


FIG. 3. Symmetry-resolved light-hole envelope functions for a [001]-growth-axis superlattice consisting of 70 Å of Ga_{0.47}In_{0.53}As alternating with 30 Å of Al_{0.48}In_{0.52}As. The energy band structure of this superlattice is shown in Fig. 1. The spin-up component (quantized along the [001] growth axis) is shown. Wave-function symmetries are defined in Appendix A. (a) First light-hole state LH₁. (b) Second light-hole states LH₂.

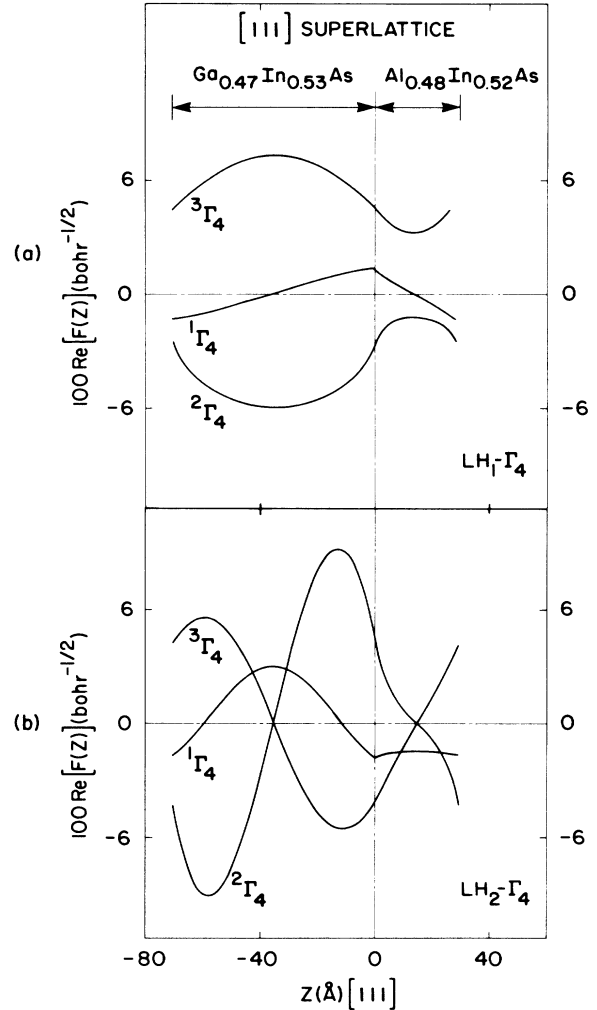


FIG. 4. Symmetry-resolved light-hole envelope functions for a [111]-growth-axis superlattice consisting of 70 Å of Ga_{0.47}In_{0.53}As alternating with 30 Å of Al_{0.48}In_{0.52}As. The energy band structure of this superlattice is shown in Fig. 2. The spin-up component (quantized along the [111]-growth axis) is shown. Wave-function symmetries are defined in Appendix A. (a) First light-hole state LH₁. (b) Second light-hole state LH₂.

the [111]-growth-axis superlattice whose dispersion curves are shown in Fig. 2. We first notice that there are no Γ_5 or Γ_6 zinc-blende periodic functions mixed into the LH_1 and LH_2 states for the [111] superlattice. The envelope function must transform like Γ_1 for [111] superlattices and therefore cannot mix Γ_5 or Γ_6 periodic functions into a Γ_4 state. The Γ_5 and Γ_6 periodic functions make up the $k_z \rightarrow 0$ heavy-hole states in the bulk material. The non-mixing of these functions into the LH_1 and LH_2 states seen in Fig. 4 corresponds to the nonmixing and band crossing of the LH_1 and HH_3 seen in the dispersion curves of Fig. 2. From Appendix A, we see that the $^1\Gamma_4$ function of the [111] superlattice is analogous to the $^1\Gamma_6$ function of the [001] superlattice, the $^2\Gamma_4$ function is analogous to the $^2\Gamma_7$ function, and the $^3\Gamma_4$ function is analogous to the $^1\Gamma_7$ function. From symmetry there are no restrictions on the envelope functions of the [111] superlattice other than that they have superlattice periodicity. However, by comparing Figs. 3 and 4, we see a very close correspondence between analogous envelope functions for the two cases.

IV. STRAINED-LAYER SUPERLATTICES

We now consider superlattices in which the bulk constituent semiconductors have slightly different lattice constants (relative difference of the order of 1–2%). In this case, high-quality epitaxial growth can be achieved provided the layers are thin enough so that the lattice mismatch is accommodated by uniform internal strain rather than by the generation of dislocations.^{6–9} The effects of lattice-mismatch-induced strain on the electronic structure of [001] semiconductor superlattices is well documented.^{7–9} In this section we emphasize differences in strain-induced effects as they relate to various growth orientations. Foremost among these differences is the presence of strain-induced internal electric fields in [111]-growth-axis strained-layer superlattices.¹⁴ These internal fields arise from piezoelectric effects and are shown to modify significantly the electronic structure and optical matrix elements of strained-layer superlattices. Such fields vanish in [001]-growth-axis strained-layer superlattices due to the symmetry properties of the strain tensor in this case.

The results presented below illustrate the effects of strain-induced piezoelectric fields on the electronic structure of [111]-growth axis $Ga_{1-x}In_xAs-Al_{1-y}In_yAs$ strained-layer superlattices. We consider the two cases where the (confining) $Ga_{1-x}In_xAs$ layers are under biaxial tension with a relative lattice mismatch of 0.8% ($x=0.53, y=0.64$) and under biaxial compression with a relative lattice mismatch of -1.5% ($x=0.53, y=0.30$). The case of a free-standing superlattice in which both semiconductors are strained is considered. The empirical parameters describing the strain Hamiltonian (deformation potential constants, elastic constants and piezoelectric constants) are listed in Table II for the systems considered here.^{32–34}

A. [111] strained-layer superlattices: Strain-induced piezoelectric fields

Lattice mismatch-induced strains do not change the symmetry of a strained-layer superlattice compared to the

TABLE II. Numerical values of deformation potential constants, elastic constants and piezoelectric constants for GaAs (=AlAs) and InAs.

Deformation potentials (eV)	GaAs (=AlAs)	InAs
c	−8.23	−5.80
b	−1.70	−1.70
d	−5.20	−5.20
Elastic constants (10^{11} dyn cm ^{−2})	GaAs (=AlAs)	InAs
C_{11}	11.81	8.33
C_{12}	5.32	4.53
C_{44}	5.92	3.96
Piezoelectric constant (C m ^{−2})	GaAs (=AlAs)	InAs
e_{14}	−0.16	−0.045

unstrained case. These strains do, however, lead to local energy-level splittings in each constituent material making up the superlattice. These energy-level splittings can be described by bulk deformation potentials for the constituent materials. As for [001] superlattices, these energy-level splittings for [111] superlattices are described by $H_{st}^{(i)}$ [see Eq. (3b)] in the Hamiltonians for the constituent materials. Bulk material deformation potentials appear in $H_{st}^{(i)}$. The strains have a different orientation for [111] superlattices than for [001] superlattices, hence $H_{st}^{(i)}$ is different for the two cases.

Strained-layer superlattices grown in the [111] direction from III-V materials have large internal electric fields which are oriented along the growth direction and have opposite polarity in the two constituent materials making up the superlattice.¹⁴ We describe these internal fields by a linearly varying potential in each of the constituent materials making up the superlattice. The approach to solving for the superlattice electronic structure in the presence of such slowly varying potentials is discussed in Appendix B.

The calculation of lattice mismatch-induced strain Hamiltonians ($H_{st}^{(i)}$) for [111]-growth-axis strained-layer superlattices proceeds in a manner similar to that of the [001] growth axis case. For [111]-growth-axis superlattices the symmetry of the problem dictates that the three diagonal strain components be equal and that the three off-diagonal strain components be equal in each material. Thus, there are four unknowns: a diagonal and an off-diagonal strain component in each material. These strain components are given in Ref. 14.³⁵

The [111] strain Hamiltonians describing local stress interactions in material i is spin-diagonal, symmetric and has upper-triangle nonvanishing matrix elements

$$\langle s | H_{st}^{[111]} | s \rangle = 3c^i e_1^i, \quad (8a)$$

$$\begin{aligned} \langle x | H_{st}^{[111]} | x \rangle &= \langle y | H_{st}^{[111]} | y \rangle = \langle z | H_{st}^{[111]} | z \rangle \\ &= (l^i + 2m^i) e_1^i, \end{aligned} \quad (8b)$$

$$\begin{aligned} \langle x | H_{st}^{[111]} | y \rangle &= \langle x | H_{st}^{[111]} | z \rangle = \langle y | H_{st}^{[111]} | z \rangle \\ &= n^i e_{||}^i, \end{aligned} \quad (8c)$$

where $e_{||}^i \equiv \epsilon_{xy}^i = \epsilon_{yz}^i = \epsilon_{zx}^i$ (Ref. 32) and $\epsilon_{\perp}^i \equiv \epsilon_{xx}^i = \epsilon_{yy}^i = \epsilon_{zz}^i$. In Eqs. (8), the constants c^i , n^i , and m^i are the deformation potential constants of semiconductor i .³⁶ The deformation potentials have been taken so that $(l^i + 2m^i) = 0$ each material. This choice fixes the ‘‘center of mass’’ of the zone-center valence-band states under the effect of the lattice-mismatch-induced internal strain.³⁷

The presence of strain in [111]-growth-axis semiconductor superlattices gives rise to internal electric fields in the strained layers due to the piezoelectric effect. Zincblende structure compound semiconductors are piezoelectric materials. Off-diagonal strains induce an electric polarization given by³⁸

$$P_i = 2e_{14}\epsilon_{jk}, \quad (9)$$

where P is the induced polarization, e_{14} is the piezoelectric constant, and ϵ_{jk} is a symmetrized strain component. However, diagonal strains (e.g., ϵ_{xx}) do not induce a polarization (i.e., $e_{11} = 0$) in these materials.³⁸ A strained-layer superlattice with a [001]-growth direction will induce only diagonal strains but with a [111]-growth direction, off-diagonal strains also occur. Thus [111]-growth-axis strained-layer superlattices will generate strain-induced polarization fields, whereas [001]-growth-axis materials will not. Because the three off-diagonal stress components are equal, the components of the polarization vector are equal and the polarization vector is in the [111] direction. The sign of the polarization vector in a material depends on whether it has the larger or smaller lattice constant and on the sign of the piezoelectric coefficient. The common III-V semiconductors have a negative piezoelectric coefficient and the common II-VI semiconductors have a positive piezoelectric coefficient.^{39,40} A III-V semiconductor with the larger lattice constant in a [111] strained-layer superlattice, will have the polarization vector pointing from the A (cation) to the B (anion) face. A III-V semiconductor with the smaller lattice constant will have the polarization point from the B to the A face. For II-VI semiconductors, the direction of the polarization vectors will be reversed. Thus, for a strained-layer superlattice with a [111]-growth axis of two III-V or two II-VI semiconductors, polarization vectors along the growth axis, and of opposite sign in the two materials, are induced by the piezoelectric effect. If one were to grow a superlattice of a III-V and a II-VI semiconductor, the polarization vectors in the two materials would have the same sign.

The strain-induced electric polarizations P_i will lead to electric fields E_i given by³⁸

$$D_i = \epsilon_0 E_i + \epsilon_0 \chi E_i + 2e_{14}\epsilon_{jk}, \quad (10)$$

where χ is the susceptibility and D_i is the electric displacement. If there are no external charges, D_i vanishes, and the electric field reduces to

$$E_i = -\frac{2e_{14}\epsilon_{jk}}{\epsilon_0\epsilon}, \quad (11)$$

where $\epsilon = 1 + \chi$ is the low-frequency dielectric constant. Application of Eq. (11) to typical III-V strained-layer superlattices, reveals that the magnitude of the strain-induced electric field is of the order of 100 kV/cm for a relative lattice-mismatch of approximately 1.5%.¹⁴ These fields are comparable to or larger than those that occur in the depletion region of a p - n junction and are approaching breakdown fields (~ 350 kV/cm in GaAs). As one would expect, the fields are larger in the thinner material because the strain is greater in that region. Although the electric fields in the two materials are of opposite sign, they do not, in general, cancel to zero. Thus, in general, the fields described by Eq. (11) consist of an alternating periodic component (that is, the potential returns to zero across a superlattice unit cell) plus a net long-range field. We assume that the long-range field will be canceled by surface charges on the superlattice sample and we treat only the effects of the periodic component on the superlattice electronic structure. We describe this periodic field by linearly varying potentials in each constituent material of the superlattice. The treatment of this linearly-varying potential is described in Appendix B.

B. Effects of strain-induced electric fields on the electronic structure of [111] superlattices

We now investigate the effects of the strain-induced electric fields on the electronic structure of [111] superlattices. We compare calculations of zone-center subband energies, subband dispersion, and wave functions with and without the electric fields. We find that the superlattice band gap is reduced⁴¹ and subband energy splittings are significantly altered by the electric fields. The subband wave functions and optical matrix elements are also strongly modified by the fields. The wave functions are displaced in space so that free carriers tend to screen the internal fields. We find that heavy holes are more effective at screening the fields than electrons or light holes. It requires a density of $\sim 10^{18}$ cm⁻³ heavy holes to reduce the internal fields by a factor of two. We are interested in the possibility of modifying the internal fields by the injection of free carriers using, for example, photoabsorption. Therefore, we present calculations as a function of the electric fields for values less than or equal to the unscreened value.

We first consider the case where the confining layers are under biaxial compression due to a lattice mismatch of -1.5% . In Fig. 5, we show the energy position of the subband levels C_1 , HH_1 , HH_2 , and LH_1 at the center of the superlattice Brillouin zone as a function of superlattice layer thickness for superlattices whose primitive cells contain an equal number of $\text{Ga}_{0.47}\text{In}_{0.53}\text{As}$ (M_a) and $\text{Al}_{0.70}\text{In}_{0.30}\text{As}$ (N_b) layers ($M_a = M_b$). An electric field of 107 kV/cm is induced in each material by the strain. Results are shown both including the strain-induced electric fields and neglecting them. The zero of energy is taken at the valence-band maximum of the strained (biaxial compression) bulk $\text{Ga}_{0.47}\text{In}_{0.53}\text{As}$ alloy at the center of the $\text{Ga}_{0.47}\text{In}_{0.53}\text{As}$ layer. In bulk $\text{Ga}_{0.47}\text{In}_{0.53}\text{As}$ in compression, the heavy-hole band is raised with respect to the light-hole band at the center of the bulk Brillouin zone.

The energy zero, the magnitude of the strain components and the magnitude of the strain-induced electric field do not change as the superlattice layer thickness is varied.

Figure 5 indicates that Stark shifts are larger for heavier particles. The Stark shifts for the heavy-hole subbands HH_1 and HH_2 have different signs at small thicknesses. These two observations are consistent with a second-order perturbation theory treatment⁴² of the Stark shifts on the bound states of a quantum well. Due to the sign of the energy denominator, the ground-state levels ($n=1$) are Stark-shifted down (towards the bottom of the

quantum well) whereas the excited states ($n>1$) are pushed up (away from the bottom of the quantum well) by the interaction with the strain-induced electric field. Also in agreement with a second-order perturbation analysis is the result that the magnitude of the Stark shift is larger for $n=1$ ground-state subband levels than for $n>1$ excited-state subband levels. The magnitude of the Stark shift increases with superlattice layer thickness, as is clearly shown in Fig. 5. This increase with superlattice layer thickness has its origin in the fact that, for a constant value of the strain-induced electric field, the electrostatic potential drop across the superlattice layers increases linearly with the thickness of the layers. At large superlattice thicknesses, the electrostatic energy (strain-induced electric field times layer thickness) is larger than

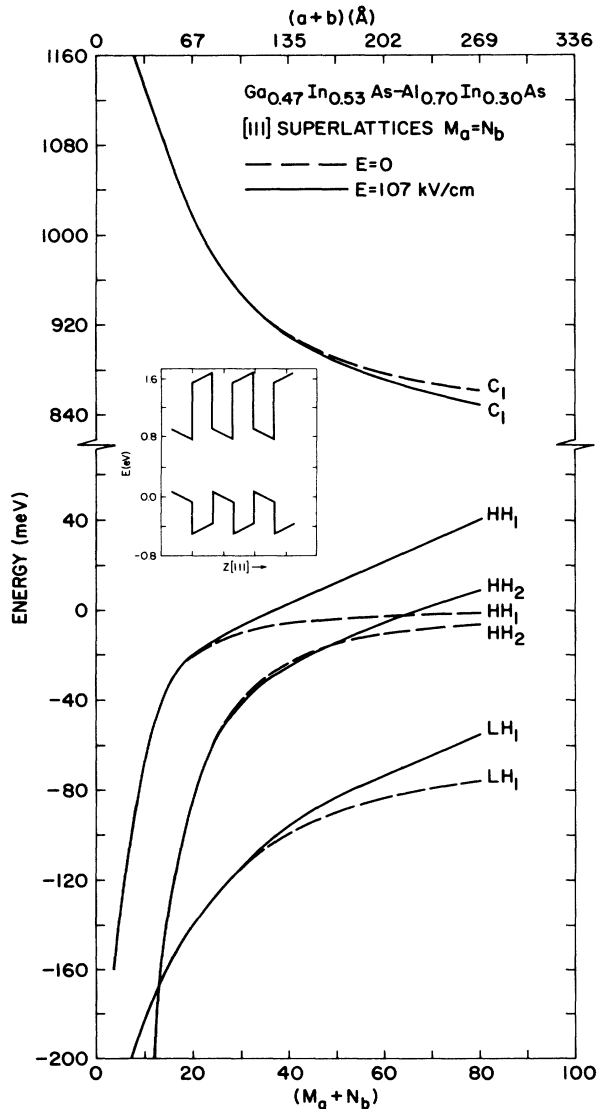


FIG. 5. Energy of zone-center subband levels as a function of superlattice layer thickness for a [111]-growth-axis strained-layer superlattice consisting of M_a layers of $Ga_{0.47}In_{0.53}As$ alternating with N_b layers of $Al_{0.70}In_{0.30}As$ ($N_b/M_a=1$). Calculations are performed with (solid lines) and without (dashed lines) the effects of strain-induced electric fields. Only the superlattice subbands HH_1 , HH_2 , LH_1 , and C_1 are shown. The inset shows the energy-band diagram of the superlattice in the presence of strain-induced electric fields.

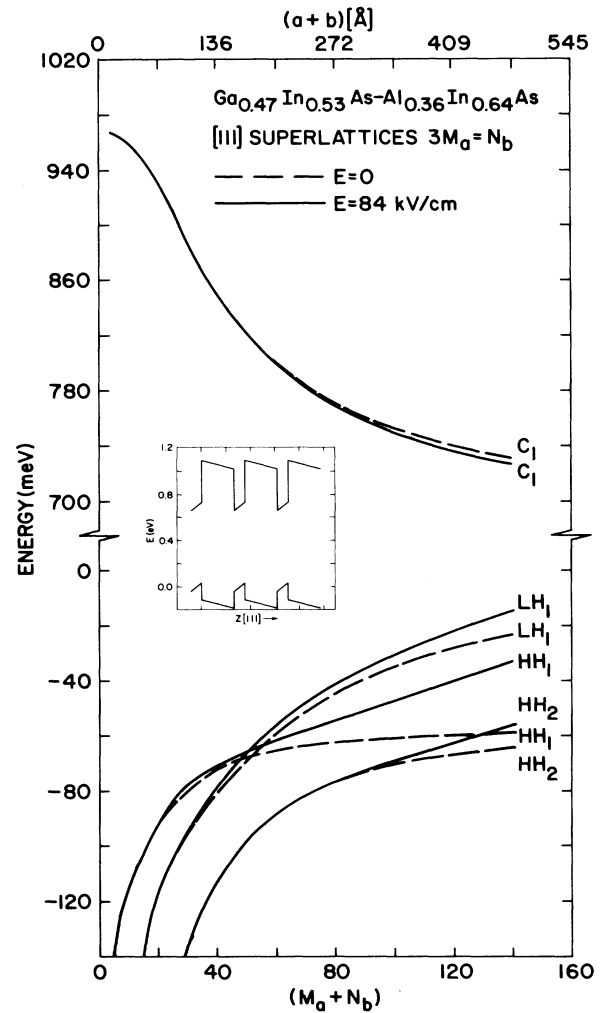


FIG. 6. Energy of zone-center subband levels as a function of superlattice layer thickness for a [111]-growth-axis strained-layer superlattice consisting of M_a layers of $Ga_{0.47}In_{0.53}As$ alternating with N_b layers of $Al_{0.36}In_{0.64}As$ ($N_b/M_a=3$). Calculations are performed with (solid lines) and without (dashed lines) the effects of strain-induced electric fields. Only the superlattice subbands HH_1 , HH_2 , LH_1 , and C_1 are shown. The inset shows the energy-band diagram of the superlattice in the presence of strain-induced electric fields.

the subband levels and the results derived from a perturbation theory treatment are no longer applicable. This is seen in Fig. 5 as the sign of the Stark shifts on the heavy-hole subbands HH_1 and HH_2 becomes the same at large superlattice periods [$(M_a + N_b) = 2M_a > 50$ layers].

We now consider the case where the confining layers are stressed under biaxial tension due to a lattice mismatch of 0.8%. Figure 6 shows the energy position of the subband levels C_1 , HH_1 , HH_2 , and LH_1 at the center of the superlattice Brillouin zone as a function of superlattice layer thickness for superlattices whose primitive cells contain three times as many $Al_{0.36}In_{0.64}As$ layers as $Ga_{0.47}In_{0.53}As$ layers ($N_b = 3M_a$). An electric field of 84 kV/cm is induced in the thinner-layer material and a field one-third of this value is induced in the thicker-layer material. Results are shown both including the strain-induced piezoelectric fields and neglecting them. The zero of energy coincides with the valence-band maximum of the strained (biaxial tension) bulk $Ga_{0.47}In_{0.53}As$ alloy at the center of the $Ga_{0.47}In_{0.53}As$ layers. In the present case, the confining $Ga_{0.47}In_{0.53}As$ layers are under biaxial tension and the light-hole band is raised with respect to the heavy-hole band at the center of the bulk Brillouin zone. A LH_1 - HH_1 strain-induced reversal occurs for a superlattice layer thickness greater than approximately $(M_a + N_b) = 4M_a > 50$ layers. The position of this strain-induced LH_1 - HH_1 crossing is fairly independent of the presence of strain-induced piezoelectric fields, as can be seen by inspection of Fig. 6. Again, heavier particles are more strongly perturbed by the presence of strain-induced piezoelectric fields than are the lighter ones, as can be seen by comparing the Stark shifts on the subbands LH_1 , C_1 , and HH_1 .

We have also analyzed the effects of strain-induced piezoelectric fields on the subband energy dispersion in the interface plane perpendicular to the [111] growth axis. The results of such an analysis are shown in Fig. 7 for the case of a [111]-growth-axis strained-layer superlattice (lattice mismatch of 1.5%) consisting of 40 layers of $Ga_{0.47}In_{0.53}As$ alternating with 40 layers of $Al_{0.70}In_{0.30}As$. Calculations are performed for $k_x \sim [1\bar{1}0]$ and $k_y \sim [11\bar{2}]$ in three cases: one case in which there are no electric fields [panel (a)], one case in which the fields are reduced to half of their unscreened values [panel (b)], and one case in which the strain-induced electric fields have their full unscreened values [panel (c)]. From Fig. 7, one sees that energy position and splittings of the highest heavy-hole subbands are significantly modified by the electric field. The effect on the dispersion is rather small, however. The masses become somewhat lighter as the electric fields are reduced from their unscreened values. However, Fig. 7 shows a case in which heavy- and light-hole zone-center energies are well separated (see Fig. 5). If the heavy- and light-hole zone-center states are close in energy, band mixing occurs and the dispersion curves become rather complicated away from the center of the superlattice Brillouin zone [see panel (a)].

An illustration of the effects of strain-induced piezoelectric fields on the superlattice wave functions is provided in Fig. 8 where the coarse grain averaged charge densities associated with the zone-center ($\mathbf{k}_{||} = \mathbf{0}, Q = 0$)

states C_1 , HH_1 , HH_2 , and LH_1 are plotted along the [111]-growth axis. The superlattice consists of 24 layers of $Ga_{0.47}In_{0.53}As$ alternating with 24 layers of $Ga_{0.70}In_{0.30}As$ grown along the [111] axis (see Fig. 5). Results including and neglecting the strain-induced electric field are compared. The electric field displaces the carrier wave functions in space. The effect is larger for the heavy-hole subbands than for the electron or light-hole subbands owing to the larger effective mass of the heavy hole. The spatial displacement of the electron and hole wave functions leads to a carrier-generated electric field

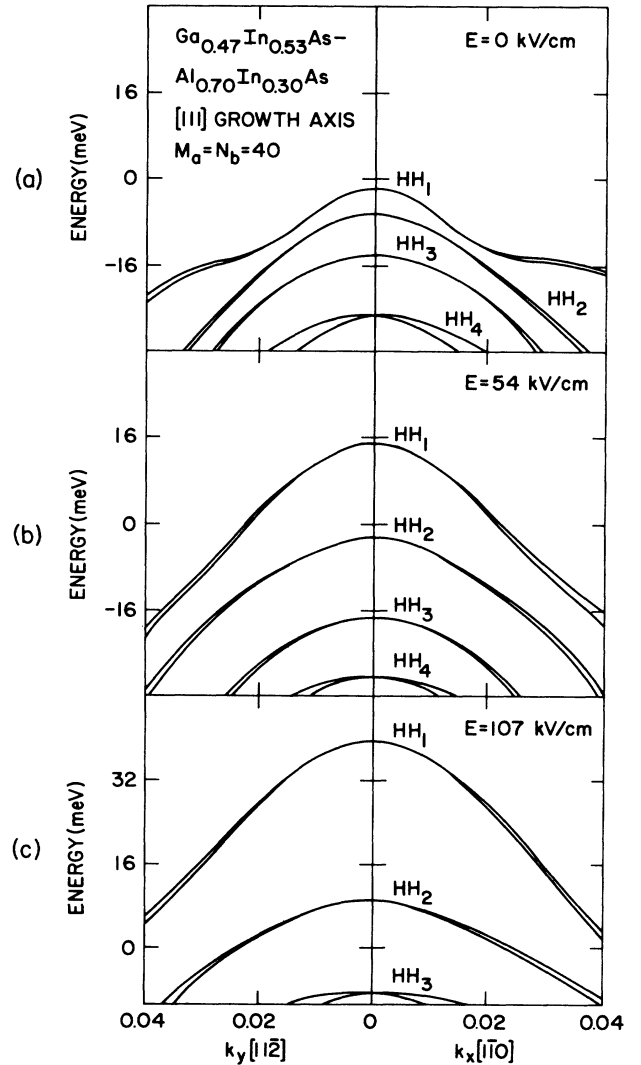


FIG. 7. In-plane energy subband dispersion for a [111]-growth-axis strained-layer superlattice consisting of 40 layers of $Ga_{0.47}In_{0.53}As$ alternating with 40 layers of $Al_{0.70}In_{0.30}As$. Energy-band structures are calculated in orthogonal directions perpendicular to the [111]-growth axis for various values of strain-induced electric field. (a) $E = 0$ kV/cm (totally screened field). (b) $E = 54$ kV/cm (partially screened field). (c) $E = 107$ kV/cm (unscreened field).

opposing the strain-induced field if both types of carriers are present due, for example, to photoabsorption. The presence of either type of free carrier alone, due, for example, to doping, will also lead to screening of the strain-induced field. The heavy holes are much more effective at screening the strain-induced fields than electrons. The

extent of the screening depends on the density of electrons and holes. In the case where the electrons and holes are generated by photoabsorption, the extent of screening and thus the photoabsorption profile becomes intensity dependent. Therefore, the strain-induced electric fields lead to a nonlinear optical response.

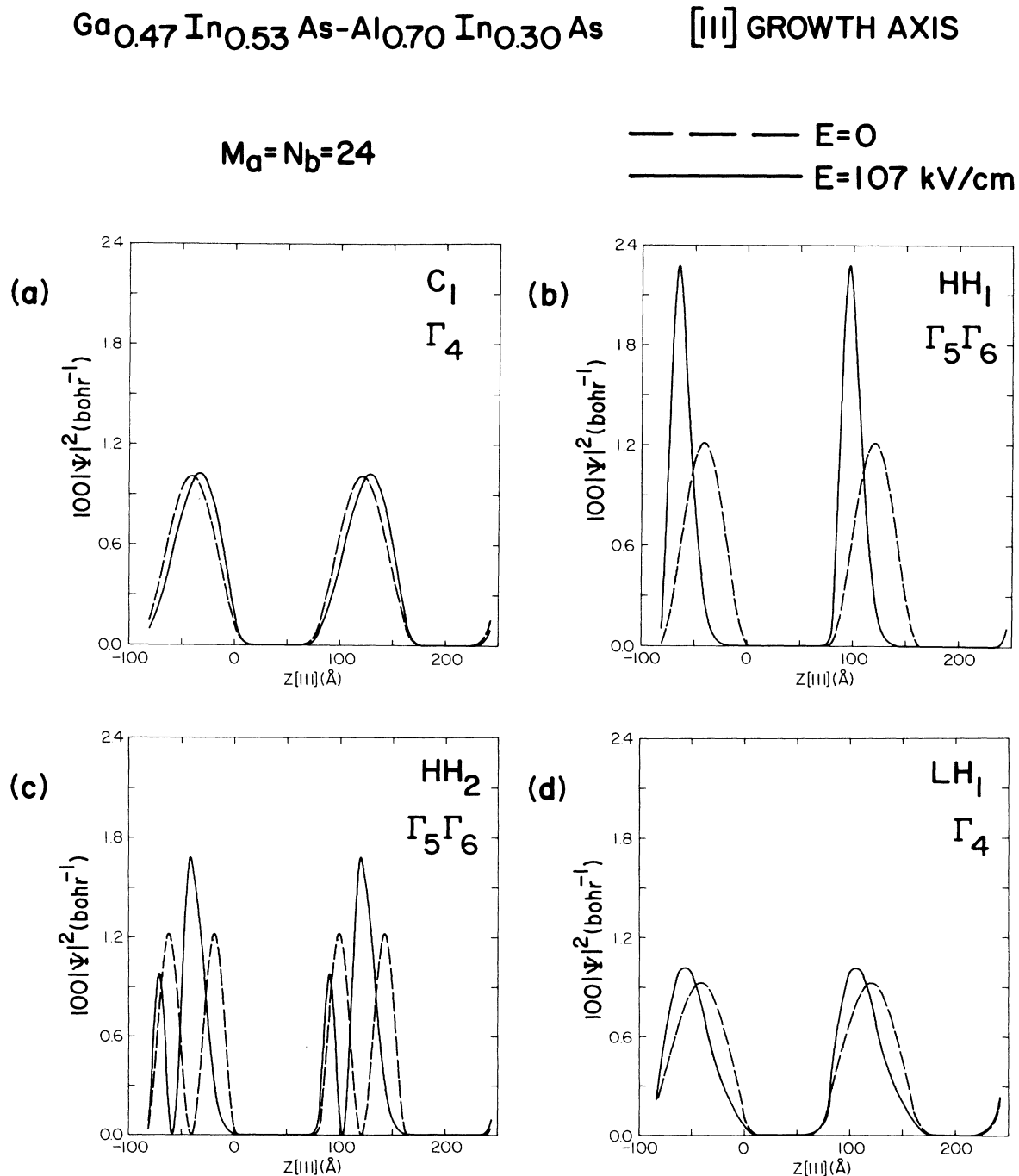


FIG. 8. Electronic charge densities for a [111]-growth-axis strained-layer superlattice consisting of 24 layers of Ga_{0.47}In_{0.53}As alternating with 24 layers of Al_{0.70}In_{0.30}As. Calculations are performed with (solid lines) and without (dashed lines) the effects of strain-induced piezoelectric fields. (a) First conduction state C₁. (b) First heavy-hole state HH₁. (c) Second heavy-hole state HH₂. (d) First light-hole state LH₁.

C. Carrier-induced screening polarization fields

We now analyze the screening polarization fields originating from the spatial separation of free carriers along the [111] growth axis of the strained-layer superlattice. In order to determine the screening polarization field arising from the field-induced spatial separation of carriers within the $\text{Ga}_{0.47}\text{In}_{0.53}\text{As}$ confining layers, we calculate the field-dependent polarization length in the confining layers of thickness a ,

$$I_n'(E) = \int_{-a}^0 dz z \left[\sum_d (|F_d^n(z)|^2 - |F_d^{n'}(z)|^2) \right], \quad (12)$$

where $F_d^n(z)$ are the envelope functions, the superscripts

n, n' refer to subband indices, and the integration is over the $\text{Ga}_{0.47}\text{In}_{0.53}\text{As}$ layer. The coordinate z is along the [111] growth axis.

The variation of $I_{\text{HH}_1}^{\text{C}_1}(E)$ as a function of strain-induced piezoelectric field strength is illustrated in Fig. 9 for various superlattice layer thicknesses ($a+b$). The screening polarization field is proportional to $I_{\text{HH}_1}^{\text{C}_1}(E)$ and is given by

$$P_{\text{screen}}(n, E) = n \frac{(a+b)}{a} e I_{\text{HH}_1}^{\text{C}_1}(E), \quad (13)$$

where n is the free carrier density, $(a+b)$ is the superlattice period, and e is the electronic charge. The electric field dependence of P_{screen} is included in the polarization length $I_{\text{HH}_1}^{\text{C}_1}(E)$. In the absence of external charges, the screened electric field E is related to the free carrier density n by the relation

$$E \left[1 + \frac{P_{\text{screen}}(n, E)}{\epsilon_0 \epsilon E} \right] = E_0, \quad (14)$$

where E_0 is the unscreened strain-induced internal field given by Eq. (11).

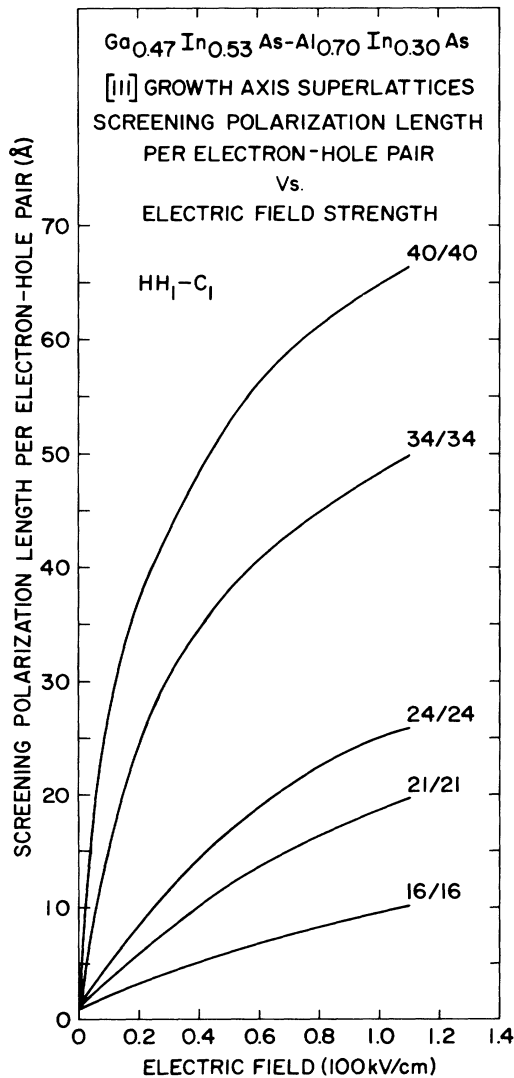


FIG. 9. Screening polarization length per electron-heavy hole pair (C_1 - HH_1) as a function of strain-induced piezoelectric field strength. Calculations correspond to a [111]-growth-axis strained-layer superlattice consisting of M_a layers of $\text{Ga}_{0.47}\text{In}_{0.53}\text{As}$ alternating with N_b layers of $\text{Al}_{0.70}\text{In}_{0.30}\text{As}$ for different values of M_a and N_b . The unscreened field is the maximum value for which calculations are performed.

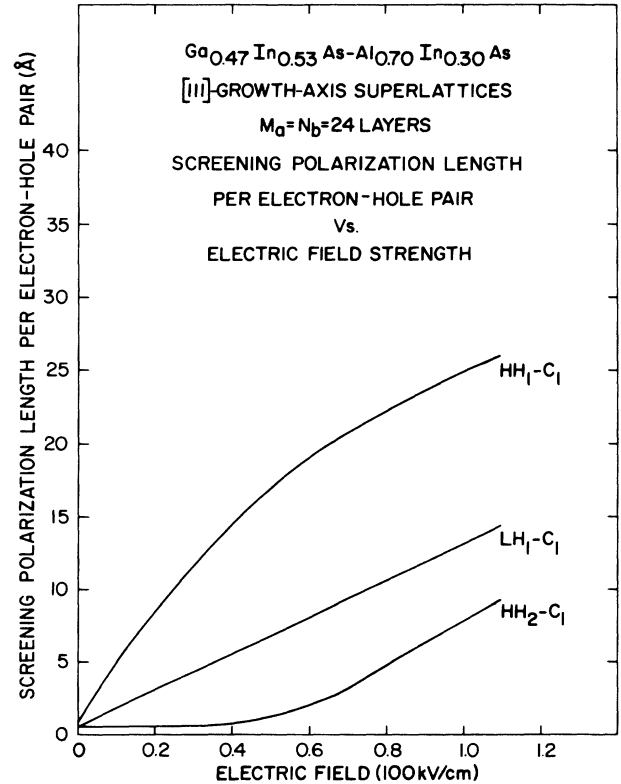


FIG. 10. Screening polarization length per electron-hole pair as a function of strain-induced piezoelectric field strength. Calculations correspond to a [111]-growth-axis strained-layer superlattice consisting of 24 layers of $\text{Ga}_{0.47}\text{In}_{0.53}\text{As}$ alternating with 24 layers of $\text{Al}_{0.70}\text{In}_{0.30}\text{As}$ for various intersubband transitions. The unscreened field is the maximum value for which calculations are performed.

The magnitude of $P_{\text{screen}}(n, E)$ increases with electric field strength and superlattice layer thickness, as indicated by Fig. 9. For a given piezoelectric field strength, the spatial separation of electrons and holes along the [111] axis is limited by thickness of the quantum wells. As the width of the $\text{Ga}_{0.47}\text{In}_{0.53}\text{As}$ layers increases, so does the screening polarization length as indicated by Fig. 9. A straightforward calculation, based on the result of Fig. 9 shows that a density of $\sim 10^{18} \text{ cm}^{-3}$ free carriers are required to reduce the internal field in the small-gap material to one-half of its unscreened value.

We have analyzed the dependence of the polarization length $I_n^n(E)$ on various superlattice subband levels. The results of such an analysis are shown in Fig. 10 where the polarization lengths $I_{\text{HH}_1}^{C_1}$, $I_{\text{HH}_2}^{C_1}$, and $I_{\text{LH}_1}^{C_1}$ are plotted as a function of strain-induced piezoelectric field strength for a [111]-growth-axis strained-layer superlattice consisting of 24 layers of $\text{Ga}_{0.47}\text{In}_{0.53}\text{As}$ alternating with 24 layers of $\text{Al}_{0.70}\text{In}_{0.30}\text{As}$. For all electric fields the inequality $I_{\text{HH}_1}^{C_1} > I_{\text{LH}_1}^{C_1} > I_{\text{HH}_2}^{C_1}$ is obeyed. This ordering can be understood by examination of the charge densities plotted in Fig. 8. Since electrons and light holes are not displaced in space as much as heavy holes by the presence of a strain-induced piezoelectric field, they give rise to smaller screening polarization fields and are therefore not as effective at screening the piezoelectric field generated by

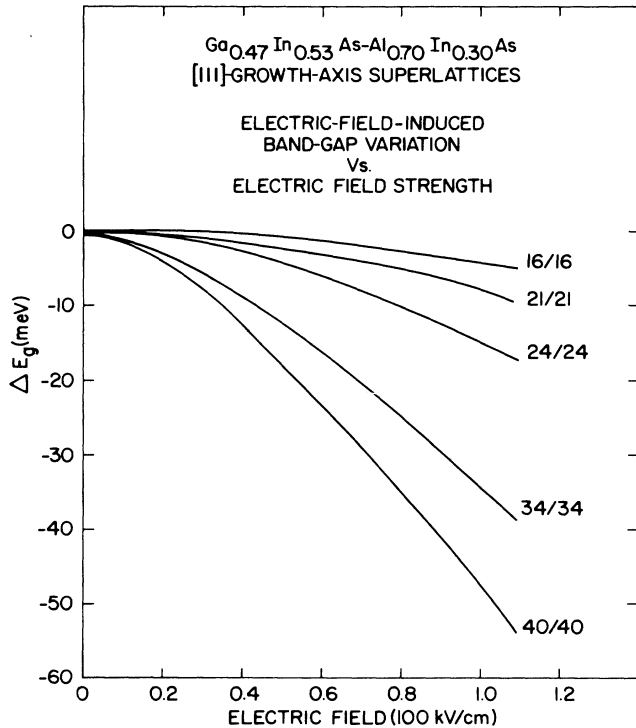


FIG. 11. Field-induced variation of the superlattice energy band gap as a function of strain-induced piezoelectric field strength. Calculations correspond to a [111]-growth-axis strained-layer superlattice consisting of M_a layers of $\text{Ga}_{0.47}\text{In}_{0.53}\text{As}$ alternating with N_b layers of $\text{Al}_{0.70}\text{In}_{0.30}\text{As}$ for different values of M_a and N_b . The unscreened field is the maximum value for which calculations are performed.

strain. Similarly, excited heavy-hole states ($\text{HH}_n, n > 1$) are more rigid than the heavy-hole ground state and are not displaced spatially as much along the [111]-growth axis.

It was shown above that the presence of strain-induced piezoelectric fields lead to sizeable reductions of the energy band gap of [111]-growth-axis strained-layer superlattices. In Fig. 11, we show the field-induced band-gap variation (band gap with field minus band gap without field) as a function of strain-induced piezoelectric field strength for a [111]-growth-axis superlattice consisting of various thicknesses of $\text{Ga}_{0.47}\text{In}_{0.53}\text{As}$ and $\text{Al}_{0.70}\text{In}_{0.30}\text{As}$. Numerical results demonstrate that the variation of the superlattice band gap is quadratic with the strain-induced piezoelectric field strength. In the context of the above discussion on carrier-induced screening of the internal polarization field, one can see that large band-gap variations (and therefore optical-absorption threshold variations) can be achieved by the generation of free carriers. Consideration of Fig. 11 indicates that this effect can be maximized if a superlattice-based device is designed to operate about an electric field for which band-gap variations respond quadratically to the field modulations.

D. Optical matrix elements

By substantially modifying the superlattice wave functions, strain-induced piezoelectric fields are expected to have dramatic effects on the optical properties of strained-layer superlattices grown along the [111] axis. In particular, both the optical matrix elements and the absorption threshold (see Sec. IV C above) are sensitive functions of the value of the strain-induced piezoelectric field. We have therefore performed calculations of the optical matrix elements at the center of the superlattice Brillouin zone ($\mathbf{k}_{\parallel} = 0, Q = 0$) as a function of the strain-induced piezoelectric field strength. We calculate the optical matrix elements to zeroth order

$$\langle n_i | \mathbf{p} | n_{i'} \rangle = \sum_{d,d'} \langle u_d | \mathbf{p} | u_{d'} \rangle \times \left[\int_{-a}^b dz [F_d^{n_i}(z)]^* F_{d'}^{n_{i'}}(z) \right], \quad (15)$$

where the sums on d are over the eight explicitly included states. We display the squared optical matrix elements defined as

$$\sum_{ii'} \frac{2}{m} |\langle n_i | \mathbf{p} \cdot \hat{\epsilon} | n_{i'} \rangle|^2, \quad (16)$$

where $|n_i\rangle$ are superlattice zone-center eigenstates, the sum on i is over the degenerate pair of eigenstates, and $\hat{\epsilon}$ is a unit polarization vector. The results of these calculations are shown in Fig. 12 for the HH_1 - C_1 transition in the case of incoming light polarized in the plane of the superlattice interfaces. This situation corresponds to the usual experimental geometry. Calculations are performed for various superlattice layer thicknesses for a [111]-growth axis $\text{Ga}_{0.47}\text{In}_{0.53}\text{As}-\text{Al}_{0.70}\text{In}_{0.30}\text{As}$ strained-layer superlattice. The spatial separation of the states HH_1 and C_1 along the [111] growth axis produced by the strain-induced electric field reduces the wave-function overlap

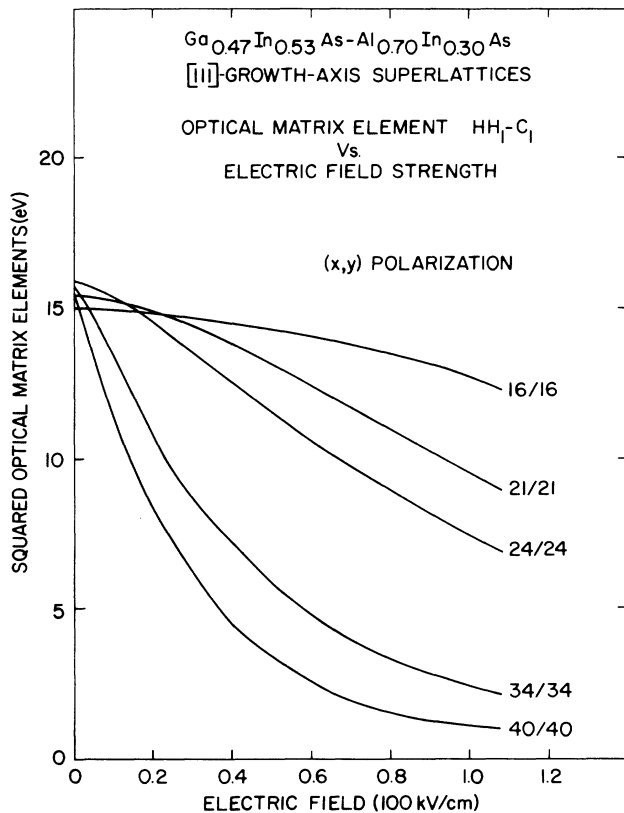


FIG. 12. Squared optical matrix element associated with a HH_1-C_1 transition as a function of strain-induced piezoelectric field strength. Calculations correspond to a [111]-growth-axis strained-layer superlattice consisting of M_a layers of $Ga_{0.47}In_{0.53}As$ alternating with N_b layers of $Al_{0.70}In_{0.30}As$ for different values of M_a and N_b . The incoming light is polarized perpendicular to the [111]-growth axis. The unscreened field is the maximum value for which calculations are performed.

and attenuates the HH_1-C_1 optical matrix element. The reduction of the optical matrix elements is more pronounced for thicker $Ga_{0.47}In_{0.53}As$ wells since the maximum separation (minimum wave-function overlap) between the states HH_1 and C_1 is ultimately governed by the quantum-well widths (assuming no tunneling through the $Al_{0.70}In_{0.30}As$ barriers). Under zero-field conditions, however, the optical matrix elements are nearly independent of superlattice layer thickness.

Figure 13 shows calculations of optical matrix elements for various optical transitions as a function of piezoelectric field strength for a [111]-growth-axis strained-layer superlattice consisting of 24 layers of $Ga_{0.47}In_{0.53}As$ alternating with 24 layers of $Al_{0.70}In_{0.30}As$. Light polarization parallel (x,y) and perpendicular (z) to the superlattice interfaces are considered. Since heavy holes are more perturbed by the presence of strain-induced piezoelectric fields, optical matrix elements corresponding to the transitions HH_1-C_1 and HH_2-C_1 are more affected by the electric field than the LH_1-C_1 transition. The presence of strain-induced electric fields alters substantially the orbital admixture and wave-function overlap of the superlattice states. As the piezoelectric field is increased, oscillation

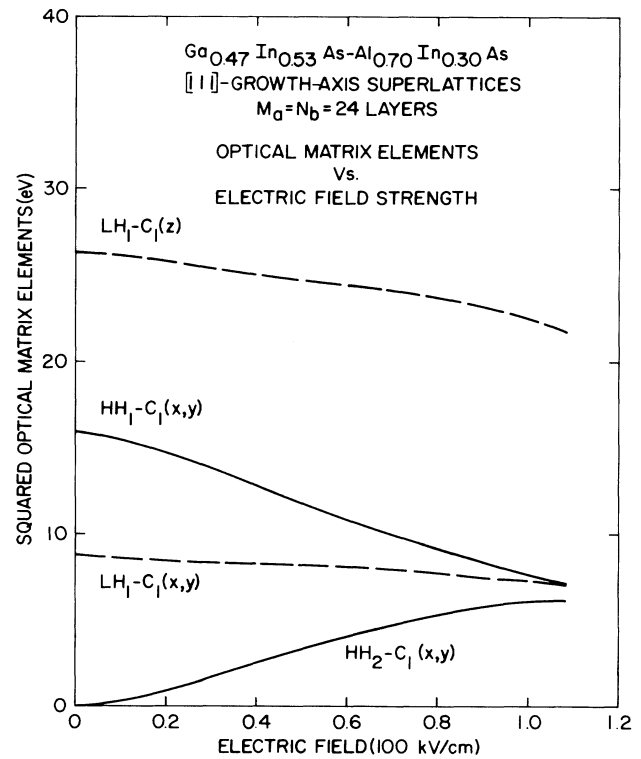


FIG. 13. Squared optical matrix elements as a function of strain-induced piezoelectric field strength. Calculations correspond to a [111]-growth-axis strained-layer superlattice consisting of 24 layers of $Ga_{0.47}In_{0.53}As$ alternating with 24 layers of $Al_{0.70}In_{0.30}As$ for various intersubband transitions. The label $z(x,y)$ refers to light polarized parallel (perpendicular) to the [111]-growth axis. The unscreened field is the maximum value for which calculations are performed.

strength is transferred from the HH_1-C_1 transition to the HH_2-C_1 transition.

V. SYNOPSIS

The electronic structure of [001]- and [111]-growth-axis $Ga_{1-x}In_xAs-Al_{1-y}In_yAs$ semiconductor superlattices is investigated with the use of a realistic $k \cdot p$ model derived from a pseudopotential scheme. Strained ($x=0.53, y=0.30$, and $x=0.53, y=0.64$) and unstrained ($x=0.53, y=0.52$) superlattices are considered. The present $k \cdot p$ model embodies a correct description of superlattice energy band splitting, mixing and crossing features and therefore permits a meaningful discussion of symmetry-related differences between [001]- and [111]-growth-axis superlattices. Apart from differences in point-group symmetry, the electronic structure of strained-layer superlattices grown along a [111] axis differ from that of [001]-growth-axis superlattices in the presence of large (exceeding 100 kV/cm) strained-induced electric fields directed along the [111]-growth axis in the latter. In [111]-growth-axis strained-layer superlattices these fields are generated by the presence of strain owing to the piezoelectric effect. Symmetry considerations forbid the presence of such fields in strained-layer superlat-

tices grown along the [001] axis. These strain-induced electric fields substantially modify the electronic structure of [111]-growth axis superlattices by causing sizeable reduction (~ 50 meV) of the superlattice band gap and producing a spatial separation of electrons and holes along the [111]-growth axis within the confining (small gap) $\text{Ga}_{0.47}\text{In}_{0.53}\text{As}$ layers. These energy-band-edge shifts modify the optical properties of strained-layer superlattices grown along the [111] axis. In particular, the absorption threshold is shifted to lower energies. The spatial separation of confined electrons and holes screens the strain-induced electric fields. The extent of the screening depends on the density of electrons and holes. In the case where the electrons and holes are generated by photoabsorption, the extent of screening and thus the photoabsorption profile, is intensity dependent. Therefore, the strain-induced electric fields lead to a nonlinear optical response. Nonlinear optical effects are maximized in configurations where the electric field strength is modulated about a point where the response varies quadratically with the amplitude of the field modulation. Screening polarization fields and interband momentum matrix elements are shown to be sensitive functions of the net internal electric field and of the superlattice layer thickness.

ACKNOWLEDGMENT

The work of D.L.S. has been financially supported by Los Alamos National Laboratory Internal Supporting Research.

APPENDIX A: SYMMETRY ANALYSIS OF ZONE-CENTER ZINC-BLENDE PERIODIC BASIS FUNCTIONS

In this appendix we construct basis functions transforming according to irreducible representations of the superlattice point group from the eight explicitly included zinc-blende periodic basis functions. We consider in turn superlattices grown along the [001] and [111] crystallographic axis.

1. [001]-growth-axis superlattices

In the case of superlattices grown along a [001] axis and having a common anion (or cation), the point group is D_{2d} . The point group D_{2d} contains two two-dimensional irreducible representations compatible with spin: Γ_6 and Γ_7 .²⁹ From the zinc-blende periodic basis functions $|s\rangle$, $|x\rangle$, $|y\rangle$, $|z\rangle$, and the two-component spinor (\uparrow, \downarrow) , we construct basis functions transforming according to the irreducible representations Γ_6 and Γ_7 of the D_{2d} point group,

$$u({}^1\Gamma_6^{1/2}) = |s\uparrow\rangle, \quad (\text{A1a})$$

$$u({}^1\Gamma_6^{-1/2}) = |s\downarrow\rangle, \quad (\text{A1b})$$

$$\sqrt{2}u({}^2\Gamma_6^{1/2}) = |i(x-iy)\downarrow\rangle, \quad (\text{A1c})$$

$$\sqrt{2}u({}^2\Gamma_6^{-1/2}) = |i(x+iy)\uparrow\rangle, \quad (\text{A1d})$$

$$u({}^1\Gamma_7^{1/2}) = |z\uparrow\rangle, \quad (\text{A1e})$$

$$u({}^1\Gamma_7^{-1/2}) = |z\downarrow\rangle \quad (\text{A1f})$$

$$\sqrt{2}u({}^2\Gamma_7^{1/2}) = |(x+iy)\downarrow\rangle, \quad (\text{A1g})$$

$$\sqrt{2}u({}^2\Gamma_7^{-1/2}) = |-(x-iy)\uparrow\rangle, \quad (\text{A1h})$$

where $x \sim [100]$, $y \sim [010]$, and z is along the [001]-growth axis.

2. [111]-growth-axis superlattices

The symmetry-point group of superlattices grown along the [111] axis is C_{3v} . The point group C_{3v} contains three irreducible representations compatible with spin. One of these irreducible representations is two-dimensional (Γ_4) whereas the other two are one-dimensional (Γ_5, Γ_6).²⁹ In constructing basis functions transforming according to the irreducible representations Γ_4 , Γ_5 , and Γ_6 of the C_{3v} point group, it is convenient to define mutually orthogonal functions referenced with respect to the [111] growth axis. We define

$$|\Phi_1\rangle \equiv \frac{1}{(2)^{1/2}}(|x\rangle - |y\rangle), \quad (\text{A2a})$$

$$|\Phi_2\rangle \equiv \frac{1}{(6)^{1/2}}(|x\rangle + |y\rangle - 2|z\rangle), \quad (\text{A2b})$$

$$|\Phi_3\rangle \equiv \frac{1}{(3)^{1/2}}(|x\rangle + |y\rangle + |z\rangle), \quad (\text{A2c})$$

where $|x\rangle$, $|y\rangle$, and $|z\rangle$ are oriented along the axes [100], [010], and [001], respectively. The functions $|\Phi_1\rangle$, $|\Phi_2\rangle$, and $|\Phi_3\rangle$ are oriented along the axes $[1\bar{1}0]$, $[11\bar{2}]$, and $[111]$, respectively. We quantize spin along [111]. Spins quantized along the [111] direction are related to those quantized along the [001] axis by the spin $-\frac{1}{2}$ transformation matrix.

With the above transformations, we construct basis functions transforming according to the Γ_4 , Γ_5 , and Γ_6 irreducible representations of the C_{3v} point group

$$u({}^1\Gamma_4^{1/2}) = |s\uparrow\rangle, \quad (\text{A3a})$$

$$u({}^1\Gamma_4^{-1/2}) = |s\downarrow\rangle, \quad (\text{A3b})$$

$$\sqrt{2}u({}^2\Gamma_4^{1/2}) = |(\Phi_1 + i\Phi_2)\downarrow\rangle, \quad (\text{A3c})$$

$$\sqrt{2}u({}^2\Gamma_4^{-1/2}) = |-(\Phi_1 - i\Phi_2)\uparrow\rangle, \quad (\text{A3d})$$

$$u({}^3\Gamma_4^{1/2}) = |\Phi_3\uparrow\rangle, \quad (\text{A3e})$$

$$u({}^3\Gamma_4^{-1/2}) = |\Phi_3\downarrow\rangle, \quad (\text{A3f})$$

$$2u(\Gamma_5) = |(\Phi_1 + i\Phi_2)\uparrow\rangle + |(\Phi_1 - i\Phi_2)\downarrow\rangle, \quad (\text{A3g})$$

$$2u(\Gamma_6) = |(\Phi_1 + i\Phi_2)\uparrow\rangle - |(\Phi_1 - i\Phi_2)\downarrow\rangle, \quad (\text{A3h})$$

where $\uparrow \equiv \uparrow_{111}$ and $\downarrow \equiv \downarrow_{111}$.

APPENDIX B: TREATMENT OF SLOWLY VARYING POTENTIALS

In this appendix, we extend our basic $\mathbf{k}\cdot\mathbf{p}$ model of the electronic structure of semiconductor superlattices²³ to include the effects of electrostatic potentials whose spatial variations are small on the scale of a bulk lattice constant. We use this approach to describe the linearly varying po-

tentials caused by stress-induced electric fields in [111] superlattices.

We consider slowly varying electrostatic potentials (no restriction is placed on the magnitude of the variation of the potential within the superlattice layers, however), divide each superlattice layer into a series of sublayers and assume that the electrostatic potential is constant within each sublayer. Let a and b be the thickness of semiconductor A and B , respectively, within a superlattice repeat cycle. Let the layer in semiconductor A (B) be divided into M (N) sublayers of thickness a_s ($s = 1, \dots, M$) [b_r ($r = 1, \dots, N$)] with

$$\sum_{s=1}^M a_s = a, \quad (\text{B1a})$$

$$\sum_{r=1}^N b_r = b. \quad (\text{B1b})$$

The energy on the sublayer s is

$$E_s = E_0 + V(s), \quad (\text{B2})$$

where E_0 is the reference energy and $V(s)$ is the value of the electrostatic potential evaluated at the center of the sublayers. We now treat each sublayer as an individual material layer and use the multilayer superlattice equations derived in Appendix D of Ref. 23. In the linearly varying potentials, we have taken the thickness of all sublayers to be equal. We have explicitly checked for numerical convergence by taking thinner sublayers.

- ¹Recent reviews on theoretical and experimental aspects of semiconductor superlattices can be found in *Proceedings of the NATO Advanced Study Institute on Molecular Beam Epitaxy and Heterostructures, Erice 1983*, edited by L. L. Chang and K. Ploog (Martinus Nijhoff, The Netherlands, 1985); *Synthetic Modulated Structure Materials*, edited by L. L. Chang and B. C. Giessen (Academic, New York, 1985).
- ²See, for example, N. Holonyak, Jr., R. M. Kolbas, R. D. Dupuis, and P. D. Dapkus, *IEEE J. Quantum Electron.* **16**, 170 (1980).
- ³D. A. B. Miller, D. S. Chemla, T. C. Damen, A. C. Gossard, W. Wiegmann, T. H. Wood, and C. A. Burrus, *Appl. Phys. Lett.* **45**, 13 (1984).
- ⁴D. S. Chemla, D. A. B. Miller, P. W. Smith, A. C. Gossard, and W. Wiegmann, *IEEE J. Quantum Electron.* **20**, 265 (1984).
- ⁵D. L. Smith, T. C. McGill, and J. N. Schulman, *Appl. Phys. Lett.* **43**, 180 (1983).
- ⁶J. W. Matthews and A. E. Blakeslee, *J. Cryst. Growth* **27**, 118 (1974); **29**, 273 (1975); **32**, 265 (1976).
- ⁷G. C. Osbourn, *J. Appl. Phys.* **53**, 1586 (1982).
- ⁸G. C. Osbourn, R. M. Biefeld, and P. L. Gourley, *Appl. Phys. Lett.* **41**, 172 (1982).
- ⁹I. J. Fritz, L. R. Dawson, and T. E. Zipperian, *Appl. Phys. Lett.* **43**, 846 (1983).
- ¹⁰W. I. Wang, T. S. Kuan, E. E. Mendez, *Phys. Rev. B* **31**, 6890 (1985).
- ¹¹J. P. Faurie, A. Million, and J. Piagnet, *Appl. Phys. Lett.* **41**, 713 (1982).
- ¹²L. A. Kolodziejcki, T. Sakamoto, R. L. Gunshor, and S. Datta, *Appl. Phys. Lett.* **44**, 799 (1984).
- ¹³R. N. Bicknell, R. Yanka, N. C. Giles-Taylor, D. K. Banks, E. L. Buckland, and J. F. Schetzina, *Appl. Phys. Lett.* **45**, 92 (1984).
- ¹⁴D. L. Smith, *Solid State Commun.* **57**, 919 (1986).
- ¹⁵J. N. Schulman and Yia-Chung Chang, *Phys. Rev. B* **33**, 2594 (1986).
- ¹⁶C. Mailhiot and D. L. Smith, *Bull. Am. Phys. Soc.* **31**, 653 (1986).
- ¹⁷R. People, K. W. Wecht, K. Alavi, and A. Y. Cho, *Appl. Phys. Lett.* **43**, 118 (1983).
- ¹⁸F. Capasso, K. Mohammed, A. Y. Cho, R. Hull, and A. L. Hutchinson, *Appl. Phys. Lett.* **47**, 420 (1985).
- ¹⁹F. Capasso, K. Mohammed, A. Y. Cho, R. Hull, and A. L. Hutchinson, *Phys. Rev. Lett.* **55**, 1152 (1985).
- ²⁰K. Shum, P. P. Ho, R. R. Alfano, D. F. Welch, G. W. Wicks, and L. F. Eastman, *Phys. Rev. B* **32**, 3806 (1985).
- ²¹W. Stolz, L. Tapfer, A. Breitschwerdt, and K. Ploog, *Appl. Phys. A* **38**, 97 (1985).
- ²²J. S. Weiner, D. S. Chemla, D. A. B. Miller, T. H. Wood, D. Sivco, and A. Y. Cho, *Appl. Phys. Lett.* **46**, 619 (1985).
- ²³D. L. Smith and C. Mailhiot, *Phys. Rev. B* **33**, 8345 (1986), and C. Mailhiot and D. L. Smith, *ibid.* **33**, 8360 (1986).
- ²⁴G. Bastard, *Phys. Rev. B* **24**, 5693 (1981); **25**, 7584 (1982).
- ²⁵S. R. White and L. J. Sham, *Phys. Rev. Lett.* **47**, 879 (1981).
- ²⁶M. Altarelli, *Phys. Rev. B* **28**, 842 (1983).
- ²⁷A. N. Pikhtin, *Fiz. Tekh. Poluprovodn.* **11**, 425 (1977) [*Sov. Phys.—Semicond.* **11**, 245 (1977)].
- ²⁸E. O. Kane, in *Physics of III-V Compounds*, edited by R. K. Williamson and A. C. Beer (Academic, New York, 1966), Vol. 1, p. 75.
- ²⁹G. F. Koster, J. O. Dimmock, R. G. Wheeler, and H. Statz, *Properties of the Thirty-two Point Groups* (MIT Press, Cambridge, 1963).
- ³⁰We use the notation of Ref. 29 to label irreducible representations of the point groups.
- ³¹For bulk zinc-blende structure compound semiconductors (T_d point group), twofold time-reversed Kramers doublets are split throughout the bulk Brillouin zone except along the fourfold [001] axis. A twofold Kramers degeneracy at a general \mathbf{k} point in the bulk Brillouin zone is ensured by a combination of time-reversal symmetry and inversion symmetry for the diamond-structure elemental semiconductors (O_h point group).
- ³²H. Mathieu, P. Merle, E. L. Ameziane, B. Archilla, and J. Camassel, *Phys. Rev. B* **19**, 2209 (1979).
- ³³R. M. Martin, *Phys. Rev. B* **1**, 4005 (1970).
- ³⁴G. D. Pitt, *Contemp. Phys.* **18**, 137 (1977).
- ³⁵There are two conventions in common use for the off-diagonal strain components, ϵ_{xy} , which differ by a factor of two. The "tensor" strain component definition, rather than the "conventional" strain component definition is used here. This is opposite to the convention used in Ref. 14, however, the results here are the same as in Ref. 14. For a clear discussion of this point, see, J. C. Hensel and G. Feher, *Phys. Rev.* **129**, 1041 (1963); in particular, see Appendix A.
- ³⁶In principle, the strains $\epsilon_{||}$ couple the $|s\rangle$ and $|x\rangle$, etc. states. However, this coupling is not important, except in very small band-gap materials, because of the large energy separation between the states.
- ³⁷In optical measurements, the deformation potential c and the combination $(l+2m)$ cannot be separately determined.

Separately specifying these numbers is equivalent to specifying a stress dependence of the energy zero. For a single material, such a specification has no physical significance. For a heterojunction system, separately specifying the deformation potential in each material specifies the stress dependence of the overall energy zero (no physical significance) and the stress dependence of the valence-band offset. There is virtually no information available on the stress dependence of valence band offsets and we have therefore adopted a reason-

able, but arbitrary prescription.

³⁸See, for example, W. F. Cady, *Piezoelectricity* (McGraw-Hill, New York, 1946).

³⁹G. Arlt and P. Q. Quadflieg, *Phys. Status Solidi* **25**, 323 (1968).

⁴⁰R. M. Martin, *Phys. Rev. B* **5**, 1607 (1972).

⁴¹C. Mailhot and D. L. Smith, *J. Vac. Sci. Technol. B* **4**, 996 (1986).

⁴²M. Matsuura and T. Kamizato, *Phys. Rev. B* **33**, 8385 (1986).